Article

Sensory neuron-derived TAFA4 promotes macrophage tissue repair functions

Guillaume Hoeffel[1,3 ✉], Guilhaume Debroas[1,3], Anais Roger[1], Rafaelle Rossignol[1], Jordi Gouilly[1], Caroline Laprie[1], Lionel Chasson[1], Pierre-Vincent Barbon[1], Anaïs Balsamo[1], Ana Reynders[2], Aziz Moqrich[2] & Sophie Ugolini[1 ✉]

Inflammation is a defence response to tissue damage that requires tight regulation in order to prevent impaired healing. Tissue-resident macrophages have a key role in tissue repair[1], but the precise molecular mechanisms that regulate the balance between inflammatory and pro-repair macrophage responses during healing remain poorly understood. Here we demonstrate a major role for sensory neurons in promoting the tissue-repair function of macrophages. In a sunburn-like model of skin damage in mice, the conditional ablation of sensory neurons expressing the Gα_i-interacting protein (GINIP) results in defective tissue regeneration and in dermal fibrosis. Elucidation of the underlying molecular mechanisms revealed a crucial role for the neuropeptide TAFA4, which is produced in the skin by C-low threshold mechanoreceptors—a subset of GINIP+ neurons. TAFA4 modulates the inflammatory profile of macrophages directly in vitro. In vivo studies in *Tafa4*-deficient mice revealed that TAFA4 promotes the production of IL-10 by dermal macrophages after UV-induced skin damage. This TAFA4–IL-10 axis also ensures the survival and maintenance of IL-10+TIM4+ dermal macrophages, reducing skin inflammation and promoting tissue regeneration. These results reveal a neuroimmune regulatory pathway driven by the neuropeptide TAFA4 that promotes the anti-inflammatory functions of macrophages and prevents fibrosis after tissue damage, and could lead to new therapeutic perspectives for inflammatory diseases.

Overexposure of the skin to UV light causes sunburn, which is characterized by destruction of the epidermis and inflammation of the underlying dermal papilla[2]. Such tissue damage induces a complex inflammatory response that requires tight regulation to prevent persistent injury. Sunburn is also characterized by a transient phase of painful hypersensitivity, which is mediated by the activation of specialized skin-innervating sensory neurons[3,4]. Studies of other pathological cutaneous conditions have shown that the peripheral nervous system regulates cutaneous inflammatory processes[3,5–9]. Most studies have focused on the roles of TRPV1+ peptidergic primary sensory neurons and the neuropeptide calcitonin gene-related peptide (CGRP)[3,5–7,9]. However, the potential immunoregulatory role of non-peptidergic C-fibres that express GINIP[10] remains unknown.

GINIP+ neurons prevent UV-induced skin fibrosis

We analysed the role of somatosensory neurons in tissue repair in mouse ears exposed to UV-C radiation—an experimental model of sunburn (Fig. 1a). We assessed the expression of genes that are associated with tissue inflammation and repair in the skin of wild-type mice after overexposure to UV. Genes that encode inflammatory molecules, such as *Il1b* and *Tnf*, were upregulated until day 7 post-UV irradiation, whereas pro-repair genes, such as *Col1a1* and *Retnla*, were upregulated

from day 14 until day 35 post-irradiation, thus defining the resolution and repair phase of this model (Extended Data Fig. 1a).

We analysed the consequences for the somatosensory nervous system of the overexposure of skin to UV light. Most of the neurons that are responsible for detecting noxious stimuli and eliciting pain perception express the sodium channel Na_v1.8[11–13], and have cell bodies in the dorsal root ganglia (DRGs) or the trigeminal ganglion. We monitored the expression of activating transcription factor 3 (ATF3), a transcription factor that is used as a proxy for neuronal injury and activation[14], in DRGs after skin exposure to UV. *Atf3* expression significantly increased in C2/C3 DRGs, which specifically innervate ear skin (Fig. 1b, Extended Data Fig. 1b–d).

We determined the phenotype of ATF3+ DRG neurons by immunofluorescence staining. Very few of these neurons co-expressed CGRP post-irradiation, whereas up to 50% co-expressed GINIP (Fig. 1c, d, Extended Data Fig. 1e, f), which suggests that UV-induced skin inflammation essentially affects GINIP+ somatosensory neurons.

We therefore investigated the role of these Na_v1.8+GINIP+ neurons (hereafter denoted GINIP+ neurons) in tissue repair through their conditional depletion in the GINIP-DTR model[10,15]. In this model, the selective ablation of GINIP+ neurons could be induced by treating the mice with diphtheria toxin (DT) (Extended Data Fig. 2a–c). Between days 5 and 35 post-irradiation, ear skin was significantly thicker in GINIP-DTR
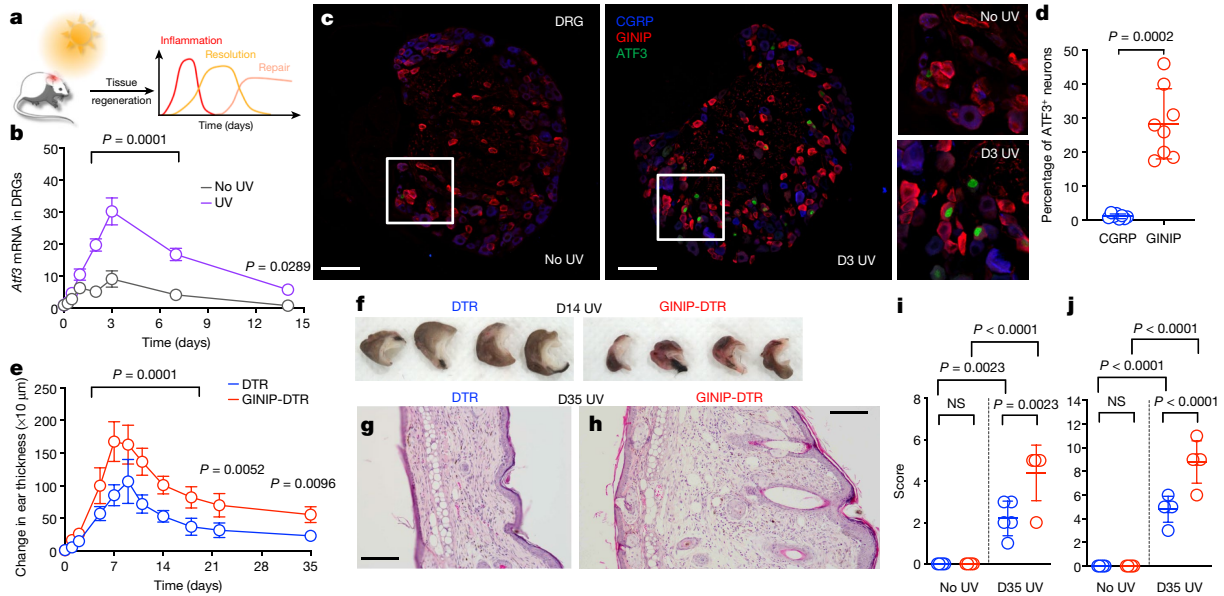
Fig. 1 | GINIP+ sensory neurons prevent fibrosis after UV exposure.
a, Experimental scheme indicating the phases of skin inflammation, resolution and repair after overexposure to UV radiation. See also Extended Data Fig. 1a for inflammatory and pro-repair gene expression post-irradiation. **b**, *Atf3* mRNA levels (arbitrary units) in C2/C3 DRGs over time in UV-irradiated (purple) and non-exposed (grey) mice ($n = 5$ mice per group). **c**, Confocal microscopy images of GINIP (red), CGRP (blue) and ATF3 (green) expression in DRGs, from unexposed (No UV) and UV-exposed (D3 (day 3) UV) mice. Scale bars, 50 μm. See also C2/C3 DRG characterization in Extended Data Fig. 1b–f. **d**, Percentage of ATF3+ neurons from C2/C3 DRGs that were positive for CGRP (blue) or GINIP (red) at D3 post-irradiation ($n = 8$ mice per group). **e**, Changes in ear thickness over time post-irradiation, in control DTR (blue) and GINIP-DTR (red) mice

($n = 7$ mice per group). **f**, Representative control DTR (left) or GINIP-DTR (right) mouse ears on D14 post-irradiation. See also neuron depletion in GINIP-DTR DRG and skin in Extended Data Fig. 2a–c. **g**, **h**, Representative haematoxylin and eosin (H&E) staining of ear sections from control DTR (**g**) and GINIP-DTR (**h**) mice at D35 post-irradiation. Scale bars, 100 μm (200× magnification). **i**, **j**, Fibrosis (**i**) and cumulative histopathological score (**j**) at D35 post-irradiation ($n = 5$ mice per group). See also Extended Data Fig. 2d–j for detailed analysis of histopathological score, scratching behaviour and back skin. Data are mean ± s.e.m. and are representative of at least two independent experiments. *P* values determined by one-way ANOVA with Tukey tests, except for **b**, **e**, two-way ANOVA and **d**, Student's *t*-test. NS, not significant.

mice than in control DTR littermates (Fig. 1e). Macroscopic analysis also revealed greater redness, tissue shrinkage and signs of necrosis, leading to loss of ear tissue in GINIP-DTR mice (Fig. 1f). These skin lesions were not associated with an increase in scratching in GINIP-DTR mice (Extended Data Fig. 2d). Histological analysis showed similar steady-state skin structures in both GINIP-DTR and control littermates. By contrast, 35 days post-irradiation, GINIP-DTR mice displayed marked pinna thickening, with an increase in horizontally oriented collagen fibre deposition, persistent leukocytic infiltration and focal auricular cartilage obliteration, whereas control mice presented signs of skin healing (Fig. 1g–j, Extended Data Fig. 2e–j). GINIP+ neurons therefore prevent skin over-inflammation and fibrosis after UV irradiation.

Impaired macrophage response in GINIP-DTR mice

We investigated whether the marked tissue repair defect of GINIP-DTR mice was linked to dysregulation of the cutaneous immune response. The absolute numbers of dendritic cells, Langerhans cells, mast cells, lymphoid cells and granulocytes were similar in GINIP-DTR and control mice, at steady state and 14 days post-irradiation, whereas GINIP−DTR mice had fewer monocytes/macrophages than control mice post-irradiation (Extended Data Fig. 3a–d). None of these immune cells expressed DTR in GINIP-DTR mice, and their numbers were unaffected by treatment with diphtheria toxin in homeostatic conditions (Extended Data Fig. 3b–d, f).

Macrophages regulate all stages of tissue repair[1], and dysregulation of their homeostasis can lead to chronic inflammation, excessive collagen deposition and hypertrophic or fibrotic scars[1]. Dermal resident macrophages that express CD206 were observed near GINIP+ nerve terminals, which suggests a possible functional interaction (Fig. 2a, b,

Extended Data Fig. 3g). We analysed the dermal monocyte/macrophage response after overexposure to UV. Tissue-resident macrophages emerge either during embryonic development[16–18] or differentiate postnatally from circulating monocytes[18,19]. Upon inflammation, monocyte subsets[20]—including 'classical' Ly6C+ monocytes, 'patrolling' Ly6Clow monocytes and 'intermediate' Ly6C+MHC-II+ monocytes—can generate short-lived MHC-II+ monocyte-derived dendritic cells and monocyte-derived CD64+CD206− inflammatory macrophages. We identified eight monocyte/macrophage subsets on the basis of differential expression of CCR2, CD64, Ly6C, MHC-II, CD206 and TIM4 (Fig. 2c, Extended Data Fig. 4a–c). Their steady-state distributions were similar in the skin of GINIP−DTR mice and control mice (Fig. 2e, f, Extended Data Fig. 4d–h). By contrast, absolute numbers of TIM4+ dermal macrophages (CD206+TIM4+) were very low from day 3 to day 14 post-irradiation in the skin of GINIP-DTR mice (Fig. 2c–e), whereas Ly6C+ monocyte recruitment increased on day 3 post-irradiation (Extended Data Fig. 4d). This influx of Ly6C+ monocytes was associated with increases in inflammatory macrophage numbers in GINIP-DTR mice from day 3 to day 14 post-irradiation (Fig. 2f), which is consistent with the stronger skin inflammation that was observed in these mice (Fig. 1e). By contrast, the expansion of CD206+ double-negative (DN; MHC-II−TIM4−) and MHC-II+ dermal macrophage subsets was little affected by the absence of GINIP+ neurons (Extended Data Fig. 4e–h). Thus, signals from GINIP+ sensory neurons promote TIM4+ dermal macrophage maintenance and control inflammatory macrophage responses after UV-induced skin damage.

TAFA4 promotes skin repair upon UV exposure

We next investigated the mechanisms that underlie the immunomodulatory and pro-repair role of GINIP+ neurons. GINIP is expressed by two
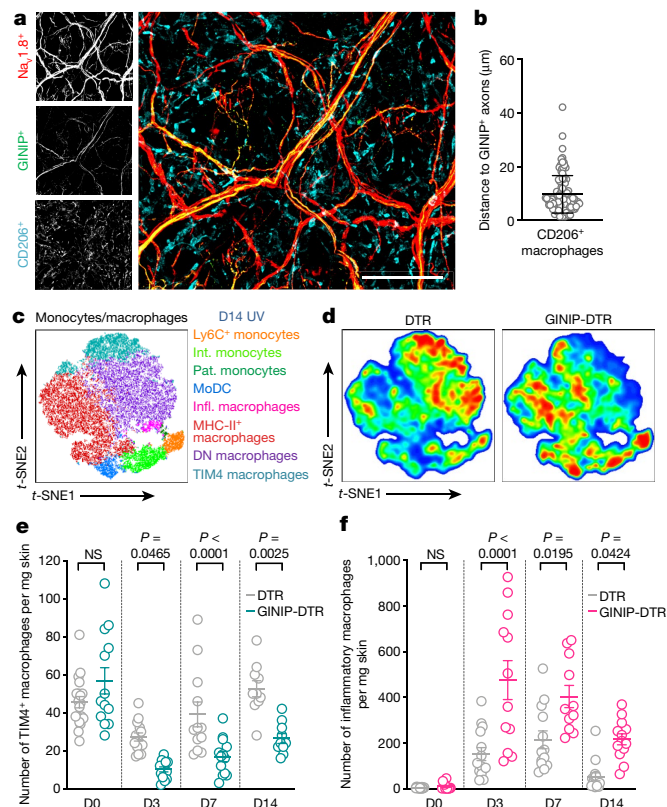
Fig. 2 | Dermal-resident TIM4⁺ macrophage maintenance is compromised in UV-exposed GINIP-DTR mice. a, Confocal microscopy analysis of ear skin (whole mount) from Na$_v$1.8-RFP mice stained for GINIP⁺ neurons (green) and CD206⁺ dermal resident macrophages (blue). Scale bar, 100 μm. The images on the left represent single channels for Na$_v$1.8RFP (top), GINIP (middle) and CD206 (bottom), which are merged and identified with a colour code on the right. See also Extended Data Fig. 3g for higher magnification. **b**, Distance between CD206⁺ macrophages and GINIP⁺ axons ($n = 97$ macrophages). **c**, Cluster analysis and t-distributed stochastic neighbour embedding (t-SNE) distribution of monocyte/macrophage subsets. Monocyte-related subsets (CCR2⁺) clustered as Ly6C⁺ monocytes (orange), intermediate (int.) monocytes (Ly6C^{int}MHC-II^{int}; light green), patrolling (pat.) monocytes (Ly6C⁻MHC-II⁻ CD64⁻; dark green) and their derivatives monocyte-derived dendritic cells (MoDC; Ly6C⁻MHC-II⁺; blue) and inflammatory (infl.) macrophages (Ly6C⁻ MHC-II⁻CD64⁺CD206⁻; pink). Dermal resident macrophage (CD64⁺CD206⁺) subsets were identified as MHC-II⁺ macrophages (MHC-II⁺TIM4⁻; red), DN macrophages (MHC-II⁻TIM4⁻; purple) and TIM4⁺ macrophages (MHC-II⁻ TIM4⁺; cyan). See also Extended Data Figs. 3a, 4a–c, e–g for the detailed gating strategy and t-SNE analysis, and Extended Data Fig. 4d–f for subset quantification. **d**, t-SNE clustering of monocyte/macrophage subsets in DTR (left) or GINIP-DTR (right) mice at D14 post-irradiation. **e**, **f**, Absolute numbers of TIM4⁺ macrophages (cyan) (**e**) or inflammatory macrophages (pink) (**f**) per mg of ear skin ($n = 10$–14 mice per group) from DTR (grey) or GINIP-DTR (coloured) mice, between day 0 and day 14 post-irradiation. Data are mean ± s.e.m. and are representative of at least two independent experiments. P values determined by one-way ANOVA with Tukey tests. NS, not significant.

somatosensory neuron subsets: GINIP⁺ neurons that bind isolectin B4 (IB4), which also express MRGPRD and selectively innervate the interfollicular region of the epidermis as free nerve endings; and GINIP⁺IB4⁻ neurons, which express TAFA4, TH and VGLUT3, markers of the C-low-threshold mechanoreceptors (C-LTMRs) that selectively innervate hair follicles[10,21] (Extended Data Fig. 5a–c). Binding to IB4 and TAFA4 expression can be used to distinguish between these subsets in DRGs[10,22,23]. We generated anti-TAFA4 monoclonal antibodies (Extended Data Fig. 5d, g) for the identification of C-LTMRs. As expected, TAFA4⁺,

TH⁺ and IB4⁺ neurons were ablated in GINIP-DTR mice, whereas CGRP⁺ neurons were spared (Extended Data Fig. 2b). DRG staining showed that 10–20% of ATF3⁺ neurons were IB4⁺ and 20–50% were TAFA4⁺ (Fig. 3a, b, Extended Data Fig. 5e, f), which suggests potential roles for these subsets of GINIP⁺ neurons in regulating UV-induced skin inflammation.

C-LTMRs mediate two opposing aspects of touch sensation: pleasantness and injury-induced mechanical pain[10,22]. TAFA4 is a secreted protein[24] that can modulate injury-induced mechanical hypersensitivity and chemical pain in mice[22]. TAFA4 promotes human macrophage chemotaxis in vitro[25], but its effect on myeloid cell responses in vivo remains unknown.

We established an ELISA for the detection of TAFA4 in tissues. Exposure to UV induced an increase in TAFA4 levels in wild-type mouse DRGs and skin (Fig. 3c, Extended Data Fig. 5h). We then investigated the cellular source of TAFA4 in skin. *Tafa4* (also known as *Fam19a4*) transcription was observed in DRGs, but not in the blood, gut, lung or skin (Extended Data Fig. 5i), which is consistent with the data for this gene in publicly available databases (https://www.immgen.org; https://biogps.org). *Tafa4* transcription has been reported in human macrophages after stimulation with lipopolysaccharide (LPS)[25]. However, we detected no *Tafa4* transcripts in bone-marrow-derived macrophages (BMDMs) activated with LPS (±TAFA4) or in sorted CD206⁺ dermal macrophages on day 0 and day 7 post-irradiation (Extended Data Fig. 5j). *Tafa4* mRNA was undetectable in the skin, even after UV exposure, but was abundant in DRGs post-irradiation (Extended Data Figs. 1a, 5k). These data strongly suggest that *Tafa4* is transcribed only in DRG neuron cell bodies, and that TAFA4 is released into the skin through C-LTMR nerve endings.

We investigated the possible role of TAFA4 in regulating tissue regeneration post-irradiation using *Tafa4*-knockout mice[22]. From day 14 to day 35 post-irradiation, *Tafa4*-knockout mice had thicker ear skin than control littermates, which suggests defective resolution of skin inflammation in the absence of TAFA4 (Extended Data Fig. 6a). No histological change in the skin of *Tafa4*-knockout mice was observed under homeostatic conditions. By contrast, at 35 days post-irradiation, leukocyte infiltration score and epidermal thickness were higher in *Tafa4*-knockout mice, which displayed more extensive, persistent dermal fibrosis than control littermates (Extended Data Fig. 6b, c). Picro-Sirius red staining revealed characteristic excessive type 1 collagen deposition in unresolved fibrotic scars in the dermis of *Tafa4*-knockout mice (Fig. 3d, e). Therefore, like GINIP-DTR mice, *Tafa4*-knockout mice presented pathological fibrosis, which suggests a requirement for the neuropeptide TAFA4—produced by C-LTMRs—in skin repair post-irradiation.

TAFA4 regulates skin macrophage IL-10 production

We next investigated the mechanisms by which TAFA4 regulates skin repair. We monitored the concentrations of inflammatory cytokines and chemokines in skin from *Tafa4*-knockout mice and control littermates from day 0 to day 35 post-irradiation. Levels of TNF, IL-1β, IL-6, CCL2, CCL4 and CXCL1 (Fig. 3f, Extended Data Fig. 6d) decreased between day 7 and day 10 post-irradiation in control mice, but remained higher in *Tafa4*-knockout mice. By contrast, expression levels of the anti-inflammatory cytokine IL-10 were lower in the skin of *Tafa4*-knockout mice post-irradiation (Fig. 3g, Extended Data Fig. 6d). Resolution of the inflammatory phase was therefore impaired in the absence of TAFA4.

IL-10 is a potent anti-inflammatory molecule. We proposed that impaired IL-10 production might underlie the observed dysregulation of skin repair in UV-exposed *Tafa4*-knockout mice. Intracellular staining and analyses in IL-10–GFP reporter mice identified resident macrophages and mast cells[26] as the main producers of IL-10, with T regulatory (T$_{reg}$) cells producing only small amounts (Extended Data Fig. 6e–i). Both the numbers of mast cells and mast-cell IL-10
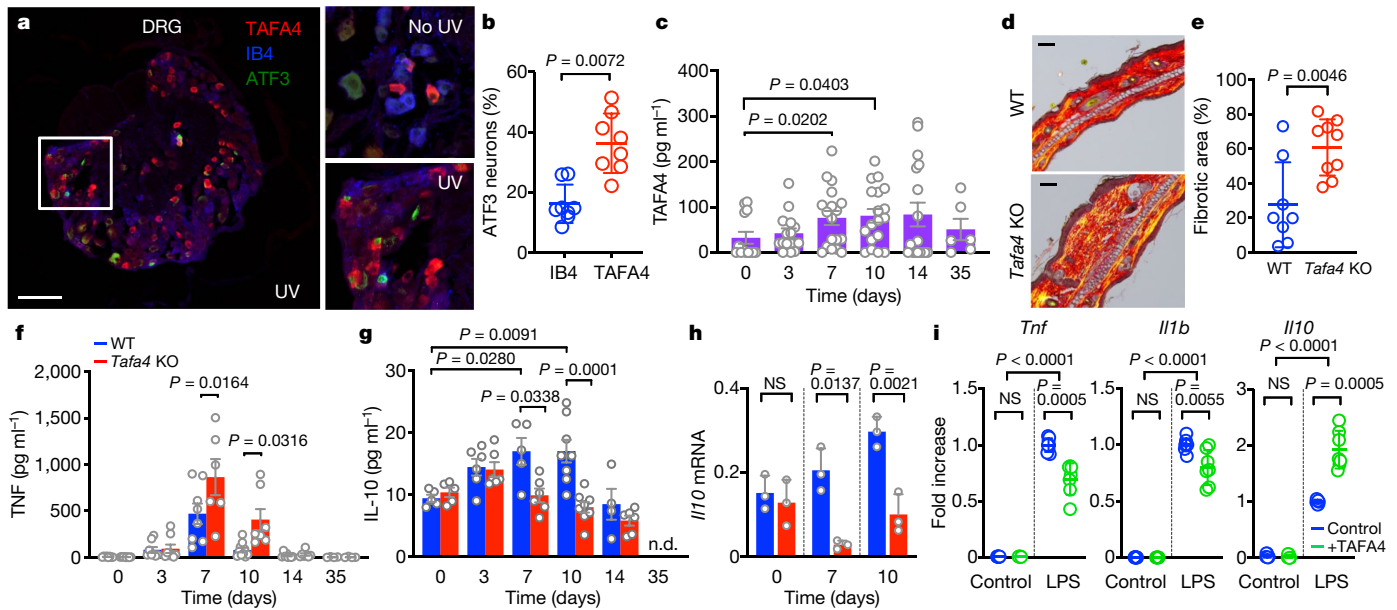
Fig. 3 | TAFA4 regulates IL-10 production by macrophages and prevents UV-induced skin fibrosis. a, Representative confocal microscopy images of C3 DRGs from wild-type mice on day 3 post-irradiation stained with IB4 (blue), anti-TAFA4 (red) and anti-ATF3 (green) antibodies. Scale bar, 50 μm. **b**, The percentage of ATF3^{+} neurons that are positive for IB4 (blue) and TAFA4 (red) (*n* = 8 mice per group). **c**, Quantification of TAFA4 (determined by ELISA) in the ear skin of wild-type mice from day 0 to day 35 post-irradiation (*n* = 6–18 mice per group). See Extended Data Fig. 5 for C-LTMR analysis and TAFA4 detection. **d**, Representative Picro-Sirius red staining of ear sections from wild-type (WT; top) and *Tafa4*-knockout (*Tafa4*-KO; bottom) mice at day 35 post-irradiation. Scale bars, 100 μm (200× magnification). **e**, The percentage of fibrosis (yellow pixels in **d**) over the total area (red + yellow pixels) (*n* = 9 mice per group). **f**, **g**, TNF (**f**) and IL-10 (**g**) levels (determined by cytometric bead array) in the ear

skin lysates of wild-type and *Tafa4*-knockout mice (*n* = 4–8 mice per group). **h**, Relative *Il10* mRNA levels in sorted dermal CD206^{+} macrophages from wild-type (blue) and *Tafa4*-knockout (red) mice between day 0 and day 10 post-irradiation (pooled from 3 independent sortings, each with *n* = 3 mice per group). **i**, Relative *Tnf*, *Il1b* and *Il10* mRNA levels (determined by quantitative PCR with reverse transcription (qRT–PCR)) for purified peritoneal macrophages (thioglycollate-elicited macrophages) activated in vitro with LPS (100 ng ml⁻¹) without (blue) or with (green) TAFA4 (100 nM) (*n* = 5–8 independent samples). Data are mean ± s.e.m. and are representative of at least two independent experiments. *P* values determined by one-way ANOVA with Tukey tests, except for **b**, **e**, Student's *t*-test; **c**, Kruskal–Wallis test. NS, not significant; **P* < 0.05; ***P* < 0.01; ****P* < 0.001.

production decreased strongly on day 3 post-irradiation (Extended Data Fig. 6j–m). TAFA4 deficiency was not associated with modulation of IL-10 production by T_reg cells and mast cells (Extended Data Fig. 6i–m). By contrast, *Il10* levels in sorted CD206^{+} dermal macrophages were lower in *Tafa4*-knockout mice than in control mice on day 7 and day 10 post-irradiation (Fig. 3h). Intracellular staining confirmed that TAFA4 was required for the upregulation of IL-10 production in all CD206^{+} macrophage subsets after overexposure to UV, and TIM4^{+} macrophages produced more IL-10 than did DN and MHC-II^{+} macrophages (Extended Data Fig. 7a–c).

We investigated whether TAFA4 regulated macrophage activation directly. BMDMs or purified peritoneal macrophages were activated with LPS in the presence or in the absence of TAFA4. *Tnf*, *Il1b* and *Il6* transcripts were significantly downregulated by TAFA4, whereas *Il10* transcripts were upregulated (Fig. 3i, Extended Data Fig. 7e, f). Together, these data suggest that the TAFA4-mediated regulation of IL-10 production in the skin upon UV exposure is mediated essentially through the regulation of dermal macrophage functions.

Formyl peptide receptor 1 (FPR1) has been described as a TAFA4 receptor that induces the chemotaxis of human macrophages and transfected cell lines in vitro[25]. We observed no chemotactic effect of TAFA4 on mouse BMDMs or isolated peritoneal macrophages in vitro (Extended Data Fig. 7d and data not shown). Consistent with this, monocyte-derived cell recruitment in vivo post-irradiation was not reduced in GINIP-DTR mice that lack TAFA4-producing C-LTMRs (Extended Data Fig. 4d). Moreover, TAFA4 had a similar immunoregulatory effect on BMDM from FPR1-knockout and wild-type mice, which demonstrates that at least one other unknown receptor drives the functional effect of TAFA4 on macrophages (Extended Data Fig. 7f).

Thus, TAFA4 can regulate the inflammatory profile of macrophages directly, in an FPR1-independent manner. It will be important to determine whether the regulation of macrophages by TAFA4 differs between mice and humans.

A TAFA4–IL-10–TIM4^{+} macrophage axis fosters healing

We then examined whether TAFA4 affected the dynamics between dermal resident macrophages and newly recruited monocyte-derived cells during repair. We first performed a lineage-tracing analysis, in which we tracked the fate of CX₃CR1^{+} embryonic macrophage precursors using the tamoxifen-dependent *CX3CR1*^CreERT2^:*R26-YFP* mouse model[27]. YFP expression was selectively induced in CX₃CR1^{+} cells on day 16.5 of embryonic development. In adult mice under homeostatic conditions, the MHC-II[+] and DN dermal macrophage subsets expressed YFP only weakly (Extended Data Fig. 8a, b). By contrast, 20% of TIM4^{+} macrophages were YFP[+], as are Langerhans cells[28], which suggests that TIM4^{+} macrophages are embryo-derived cells.

We then assessed the contribution of monocytes to the various dermal monocyte subsets by generating shield-irradiated bone marrow chimeras (Extended Data Fig. 8c). As expected, two months after CD45.1 bone marrow reconstitution in CD45.2 recipients, 90% of blood monocytes were CD45.1[+], whereas microglia were entirely of recipient (CD45.2[+]) origin (Extended Data Fig. 8c). Under homeostatic conditions, dermal Ly6C^{+} monocytes, intermediate monocytes, patrolling monocytes, monocyte-derived dendritic cells and inflammatory macrophages were mostly CD45.1[+], which confirmed their origin in the bone marrow; by contrast, TIM4^{+} macrophages were CD45.2[+], demonstrating their self-maintenance over time, independently of
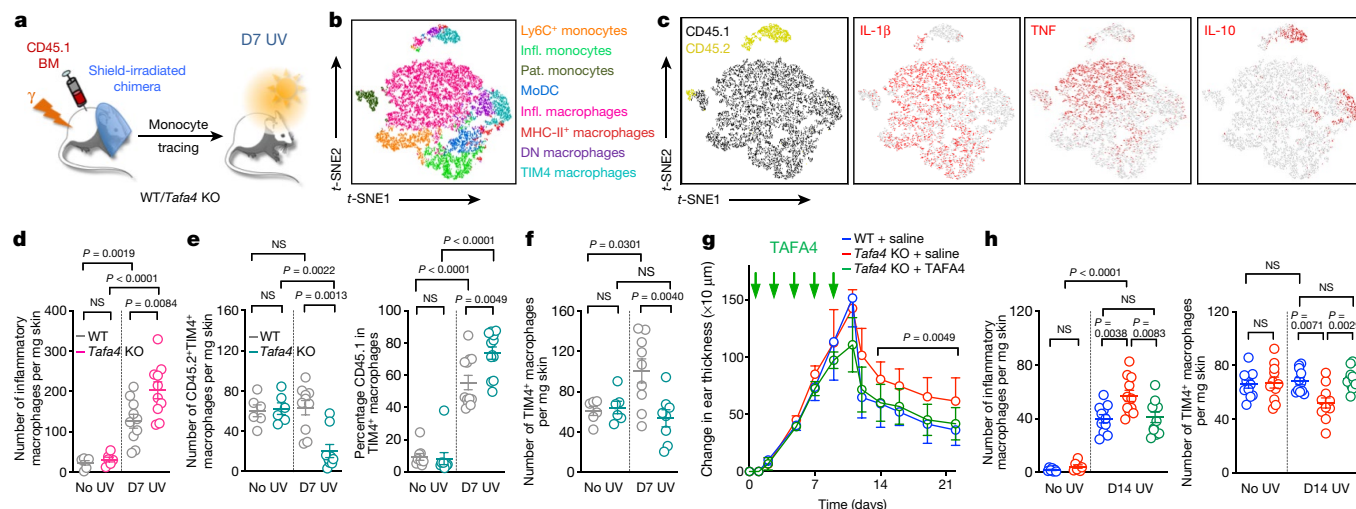
Fig. 4 | The TAFA4–IL-10 axis promotes TIM4+ macrophage survival and tissue repair functions. a, Experimental strategy for generating CD45.1 bone-marrow chimeras in CD45.2 wild-type or *Tafa4*-knockout recipient mice and monitoring monocyte-derived cells post-irradiation. **b**, Fluorescence-activated cell sorting (FACS) and *t*-SNE analysis of skin monocyte/macrophage subsets 7 days post-irradiation, as described in Fig. 2; see also Extended Data Fig. 8f–h for detailed analysis of bone-marrow chimeras. **c**, *t*-SNE analysis of CD45.2+ (yellow) and CD45.1+ (black) clusters and intracellular staining for IL-1β, TNF and IL-10 (red). **d**, Absolute numbers of inflammatory macrophages in wild-type control (grey) and *Tafa4*-knockout (pink) bone-marrow-chimeric mice. **e**, Left, absolute numbers of CD45.2+TIM4+ macrophages; and right, percentage of CD45.1 chimerism in total TIM4+ macrophages from wild-type

(grey) and *Tafa4*-knockout (cyan) bone-marrow-chimeric mice. **f**, Absolute numbers of total (CD45.1+ and CD45.2+) TIM4+ macrophages in wild-type (grey) and *Tafa4*-knockout (cyan) bone-marrow-chimeric mice ($n = 6$–10 mice per group). **g**, Intradermal TAFA4 injection in *Tafa4*-knockout mice (green arrows) and changes in ear thickness over 21 days post-irradiation in saline-treated wild-type (blue) and *Tafa4*-knockout (red) mice, or *Tafa4*-knockout mice treated with TAFA4 (green) ($n = 14$ mice per group). **h**, Absolute numbers of inflammatory macrophages (left) and TIM4+ macrophages (right) in ear skin on day 14 post-irradiation ($n = 11$ mice per group). Data are mean ± s.e.m. and are representative of at least two independent experiments. P values determined by one-way ANOVA with Tukey tests except for **g**, two-way ANOVA. NS, not significant; *$P < 0.05$; **$P < 0.01$; ***$P < 0.001$.

circulating monocytes (Extended Data Fig. 8d). However, 120 days post-irradiation, the CD45.1 chimerism of DN and TIM4+ macrophages increased (Extended Data Fig. 8e), showing that monocytes recruited post-irradiation acquired a resident-like macrophage phenotype with self-renewing capacity.

We then generated shield-irradiated bone marrow chimeras, using wild-type or *Tafa4*-knockout (both CD45.2) recipient mice (Fig. 4a–f, Extended Data Fig. 8f–h). Intracellular staining on day 7 post-irradiation revealed that IL-1β expression was mostly associated with monocyte-derived cells, whereas TNF expression was restricted essentially to inflammatory macrophages (Fig. 4c). The number of inflammatory macrophage cells in *Tafa4*-knockout chimeric mice was higher than that in control chimeras, suggesting that TAFA4 reduces the number of newly derived inflammatory macrophages (Fig. 4d). TIM4+ macrophages were the predominant CD45.2+ population in both chimeras (Fig. 4b, c), consistent with our previous analysis. TIM4+ macrophages produced large amounts of IL-10, but no IL-1β or TNF (Fig. 4c), highlighting their anti-inflammatory function. TAFA4 deficiency had little effect on DN and MHC-II+ macrophage homeostasis post-irradiation (Extended Data Fig. 8h). By contrast, the absolute number of CD45.2+TIM4+ macrophages, which was similar in both chimeras under homeostatic conditions, strongly decreased in *Tafa4*-knockout recipient mice post-irradiation (Fig. 4e, left). Overall CD45.1 chimerism levels in TIM4+ macrophages revealed that CD45.2+TIM4+ macrophages were replaced by CD45.1+ monocyte differentiation to a greater extent in *Tafa4*-knockout than in wild-type recipients (Fig. 4e, right). However, the overall TIM4+ macrophage pool expanded to a lesser extent in the absence of TAFA4 (Fig. 4f), which suggests that both embryo-derived and monocyte-derived TIM4+ macrophages require TAFA4 for survival post-irradiation. Consistently, the frequency of apoptotic annexin+TIM4+ cells in UV-exposed skin was higher for GINIP-DTR and *Tafa4*-knockout mice than for control littermates, whereas DN and MHC-II+ subsets were unaffected (Extended Data Fig. 8i–l). Thus, after exposure to UV, both GINIP-DTR and *Tafa4*-knockout mice present

an imbalanced macrophage response, and show impaired survival of IL-10-producing TIM4+ macrophages and larger numbers of inflammatory macrophages. TAFA4 deficiency therefore affects both the maintenance of dermal TIM4+ macrophages and their capacity to produce IL-10.

Intradermal injections of IL-10-blocking antibodies before UV irradiation in wild-type mice induced a phenotype similar to that of *Tafa4*-knockout mice (Extended Data Fig. 9a–c), which suggests that IL-10 upregulation is essential for the maintenance of TIM4+ macrophages. Similarly, IL-10-deficient mice (*IL-10*GFP/GFP mice) exposed to UV had smaller numbers of TIM4+ macrophages, larger numbers of inflammatory macrophages and greater skin damage (Extended Data Fig. 9d–f). IL-10 defects are, therefore, sufficient to mimic the phenotype of GINIP-DTR and *Tafa4*-knockout mice, which suggests that IL-10 acts downstream from TAFA4 signalling.

Consistent with the role of IL-10-producing macrophages in this model, we found that the depletion of resident macrophages by treatment with CSF-1R-blocking antibody (AFS98)[17] before UV exposure decreased the total content of IL-10 in the skin (Extended Data Fig. 9g–j). Monocyte infiltration after resident macrophage depletion led to the rapid reconstitution of MHC-II+ and DN macrophage subsets, whereas the generation of TIM4+ macrophages took up six days (Extended Data Fig. 9k). Mice deficient in resident macrophages showed increases both in the number of inflammatory macrophages and in skin damage post-irradiation (Extended Data Fig. 9l–n), which demonstrates the requirement of a TAFA4–dermal resident macrophage axis for the regulation of inflammatory macrophage responses. Furthermore, adoptive transfer of sorted dermal TIM4+ macrophages in the skin of GINIP-DTR mice post-irradiation was sufficient to limit tissue damage (Extended Data Fig. 10a–d). Thus, the early loss of dermal resident TIM4+ macrophages determines the rates of tissue damage and of impaired healing in GINIP-DTR and *Tafa4*-knockout mice.

Finally, the phenotype of *Tafa4*-knockout mice was rescued by intradermal injections of recombinant TAFA4 post-irradiation (Fig. 4g, h).

TAFA4 administration was also sufficient to upregulate IL-10 production by TIM4^{+} macrophages in *Tafa4*-knockout mice (Extended Data Fig. 10e, f). These data suggest that TAFA4 production by C-LTMR nerve endings after UV exposure is necessary and sufficient to downregulate inflammatory processes by modulating dermal macrophage homeostasis and IL-10 production.

Discussion

This study reveals an immunoregulatory role of non-peptidergic GINIP[+] cutaneous sensory neurons in tissue repair through the production of TAFA4, which promotes early and persistent IL-10 production by dermal macrophages. TAFA4 ensures the survival of embryo-derived TIM4^{+} macrophages and sustains their production of large amounts of IL-10. This neuroimmune pathway downregulates the expansion of inflammatory macrophages, thereby reducing levels of inflammatory cytokines and promoting skin repair (Extended Data Fig. 10g). These data are consistent with the metabolic reprograming capacity[29] of IL-10 and with previous reports of IL-10 deficiency leading to excessive collagen deposition during wound healing[30]. The regulatory role of TAFA4 is not limited to TIM4^{+} macrophages. TAFA4 can also modulate the inflammatory profile of other macrophage subsets in vitro and in vivo, including other CD206^{+} dermal macrophage subsets and peritoneal macrophages.

Recent studies involving the genetic or chemical ablation of sensory neuron subsets have revealed a regulatory role of the somatosensory nervous system in cutaneous immune responses[3,5–9], which could be pro- or anti-inflammatory. The considerable functional and phenotypic heterogeneity of somatosensory neurons[31–33], and their selective or combinatorial stimulation, could account for immunoregulatory differences between pathological contexts. Previous studies have identified an important role for TRPV1^{+} neurons and the neuropeptide CGRP in bacterial and fungal infections and in models of sterile and imiquimod-induced cutaneous inflammation[3,5–7,9]. Our study reveals that TAFA4 production by C-LTMRs has an important immunomodulatory role in a sunburn-like model of skin damage. By contrast, no such effect was observed in a model of imiquimod-induced skin inflammation (Extended Data Fig. 10h). It will therefore be important to determine whether this neuroimmune regulatory pathway also has a role in other skin pathological contexts. The properties of TAFA4 could be exploited therapeutically to modulate inflammation in other inflammatory diseases or in patients with wound-healing defects.

Online content

Any methods, additional references, Nature Research reporting summaries, source data, extended data, supplementary information, acknowledgements, peer review information; details of author contributions and competing interests; and statements of data and code availability are available at https://doi.org/10.1038/s41586-021-03563-7.

1. Wynn, T. A. & Vannella, K. M. Macrophages in tissue repair, regeneration, and fibrosis. *Immunity* **44**, 450–462 (2016).
2. Merad, M. et al. Langerhans cells renew in the skin throughout life under steady-state conditions. *Nat. Immunol.* **3**, 1135–1141 (2002).
3. La Russa, F. et al. Disruption of the sensory system affects sterile cutaneous inflammation in vivo. *J. Invest. Dermatol.* **139**, 1936–1945.e3 (2019).
4. Lopes, D. M. & McMahon, S. B. Ultraviolet radiation on the skin: a painful experience? *CNS Neurosci. Ther.* **22**, 118–126 (2016).
5. Chiu, I. M. et al. Bacteria activate sensory neurons that modulate pain and inflammation. *Nature* **501**, 52–57 (2013).
6. Riol-Blanco, L. et al. Nociceptive sensory neurons drive interleukin-23-mediated psoriasiform skin inflammation. *Nature* **510**, 157–161 (2014).
7. Kashem, S. W. et al. Nociceptive sensory fibers drive interleukin-23 production from CD301b^{+} dermal dendritic cells and drive protective cutaneous immunity. *Immunity* **43**, 515–526 (2015).
8. Pinho-Ribeiro, F. A. et al. Blocking neuronal signaling to immune cells treats streptococcal invasive infection. *Cell* **173**, 1083–1097.e22 (2018).
9. Cohen, J. A. et al. Cutaneous TRPV1^{+} neurons trigger protective innate type 17 anticipatory immunity. *Cell* **178**, 919–932.e14 (2019).
10. Gaillard, S. et al. GINIP, a G$_{αi}$-interacting protein, functions as a key modulator of peripheral GABAB receptor-mediated analgesia. *Neuron* **84**, 123–136 (2014).
11. Basbaum, A. I., Bautista, D. M., Scherrer, G. & Julius, D. Cellular and molecular mechanisms of pain. *Cell* **139**, 267–284 (2009).
12. Abraira, V. E. & Ginty, D. D. The sensory neurons of touch. *Neuron* **79**, 618–639 (2013).
13. Abrahamsen, B. et al. The cell and molecular basis of mechanical, cold, and inflammatory pain. *Science* **321**, 702–705 (2008).
14. Bráz, J. M. & Basbaum, A. I. Differential ATF3 expression in dorsal root ganglion neurons reveals the profile of primary afferents engaged by diverse noxious chemical stimuli. *Pain* **150**, 290–301 (2010).
15. Urien, L. et al. Genetic ablation of GINIP-expressing primary sensory neurons strongly impairs formalin-evoked pain. *Sci. Rep.* **7**, 43493 (2017).
16. Gomez Perdiguero, E. et al. Tissue-resident macrophages originate from yolk-sac-derived erythro-myeloid progenitors. *Nature* **518**, 547–551 (2015).
17. Hoeffel, G. et al. C-Myb[+] erythro-myeloid progenitor-derived fetal monocytes give rise to adult tissue-resident macrophages. *Immunity* **42**, 665–678 (2015).
18. Hoeffel, G. & Ginhoux, F. Fetal monocytes and the origins of tissue-resident macrophages. *Cell. Immunol.* **330**, 5–15 (2018).
19. Ginhoux, F. & Jung, S. Monocytes and macrophages: developmental pathways and tissue homeostasis. *Nat. Rev. Immunol.* **14**, 392–404 (2014).
20. Guilliams, M., Mildner, A. & Yona, S. Developmental and functional heterogeneity of monocytes. *Immunity* **49**, 595–613 (2018).
21. Li, L. et al. The functional organization of cutaneous low-threshold mechanosensory neurons. *Cell* **147**, 1615–1627 (2011).
22. Delfini, M. C. et al. TAFA4, a chemokine-like protein, modulates injury-induced mechanical and chemical pain hypersensitivity in mice. *Cell Rep.* **5**, 378–388 (2013).
23. Reynders, A. et al. Transcriptional profiling of cutaneous MRGPRD free nerve endings and C-LTMRs. *Cell Rep.* **10**, 1007–1019 (2015).
24. Tang, Y. T. et al. TAFA: a novel secreted family with conserved cysteine residues and restricted expression in the brain. *Genomics* **83**, 727–734 (2004).
25. Wang, W. et al. FAM19A4 is a novel cytokine ligand of formyl peptide receptor 1 (FPR1) and is able to promote the migration and phagocytosis of macrophages. *Cell. Mol. Immunol.* **12**, 615–624 (2015).
26. Grimbaldeston, M. A., Nakae, S., Kalesnikoff, J., Tsai, M. & Galli, S. J. Mast cell-derived interleukin 10 limits skin pathology in contact dermatitis and chronic irradiation with ultraviolet B. *Nat. Immunol.* **8**, 1095–1104 (2007).
27. Yona, S. et al. Fate mapping reveals origins and dynamics of monocytes and tissue macrophages under homeostasis. *Immunity* **38**, 79–91 (2013).
28. Hoeffel, G. et al. Adult Langerhans cells derive predominantly from embryonic fetal liver monocytes with a minor contribution of yolk sac-derived macrophages. *J. Exp. Med.* **209**, 1167–1181 (2012).
29. Ip, W. K. E., Hoshi, N., Shouval, D. S., Snapper, S. & Medzhitov, R. Anti-inflammatory effect of IL-10 mediated by metabolic reprogramming of macrophages. *Science* **356**, 513–519 (2017).
30. Eming, S. A. et al. Accelerated wound closure in mice deficient for interleukin-10. *Am. J. Pathol.* **170**, 188–202 (2007).
31. Cavanaugh, D. J. et al. Distinct subsets of unmyelinated primary sensory fibers mediate behavioral responses to noxious thermal and mechanical stimuli. *Proc. Natl Acad. Sci. USA* **106**, 9075–9080 (2009).
32. Usoskin, D. et al. Unbiased classification of sensory neuron types by large-scale single-cell RNA sequencing. *Nat. Neurosci.* **18**, 145–153 (2015).
33. Sharma, N. et al. The emergence of transcriptional identity in somatosensory neurons. *Nature* **577**, 392–398 (2020).

Article

Methods

No statistical methods were used to predetermine sample size. The experiments were not randomized and the investigators were not blinded to allocation during experiments and outcome assessment unless otherwise stated.

Mice

C57/BL6J mice were bought from Janvier Labs (https://www.janvier-labs.com). GINIP-DTR mice were obtained by crossing *GINIP*[flx/+] line[10] with mice expressing the Cre recombinase from the *Nav1.8* (otherwise known as *Scn10a*) locus (*Nav1.8*[Cre/Cre] mice)[13]. One single diphtheria toxin (10 µg kg^{-1}) injection in 4-week-old *Nav1.8*[Cre/+]*GINIP*[flx/+] (hereafter called GINIP-DTR mice) enabled the specific ablation of GINIP^{+} sensory neurons[15]. *Nav1.8*[+/+]*GINIP*[flx/+] littermates (hereafter called DTR mice) treated with diphtheria toxin were used as controls throughout. *Nav1.8*[RFP] mice were obtained by crossing *Nav1.8*[Cre/+] with *flxR26-RFP* mice. Homozygotes *IL-10*[GFP/GFP] mice, described previously[34,35], were provided by S. Memet and J. P. Gorvel (CIML) and used with their heterozygotes *IL-10*[GFP/WT] control littermates. *Tafa4*-knockout mice were generated in the laboratory of A.M. (IBDM, France) and described previously[22]. *CX3CR1*[CreERT2]:*R26-YFP* mice were described previously[27] and were provided by S. Sarrazin and M. Sieweke (CIML). All the mice used were bred and maintained under specific-pathogen-free conditions at the Centre d'Immunophénomique (Ciphe) de Marseille and at the Centre d'Immunologie de Marseille Luminy (CIML). Mice were housed under a standard 12 h:12 h light:dark cycle with ad libitum access to food and water. Age-matched (6–12 weeks old, unless otherwise specified) and sex-matched littermate mice were used as controls. All experiments were conducted in accordance with institutional committee recommendations (Comité d'Éthique de Marseille no. 14-APAFiS, 18469-2019011417196625v2) and French and European guidelines for animal care.

Bone marrow chimera generation

Age and sex matched wild-type or *Tafa4*-knockout mice (CD45.2[+]) were anaesthetized with ketamine/xylazine (10 µl g^{-1}, 2% imalgene500/5% rompun). Mice were then irradiated with a dose of 6.5 Gy from an γ-ray irradiator. A lead shield was used to protect the skin of the ear from γ-irradiation. Six hours after irradiation, 30 mg kg^{-1} busulfan (Sigma)[36] was injected (i.p.) to deplete remaining myeloid progenitors in recipient mice. Twelve hours later the mice were reconstituted with 5 million CD45.1[+] bone marrow cells. Mice were treated with Bactrim (in drinking water) for two weeks for a total recovery time of 6 weeks before analysing the blood CD45.1 chimerism, and were then used for experiments.

Lineage tracing study

CX3CR1[CreERT2:R26R-eYFP+/+] mice were used as described[27]. Tamoxifen (2 mg tamoxifen per mouse; 40 mg ml^{-1} in corn oil; Sigma) was injected i.p. to pregnant mice 16.5 days after conception. The day of embryonic development (E) was estimated by taking the day on which a vaginal plug was observed as E0.5. Caesarian sections were carried out at term and neonates were fostered by lactating females. In this model, tamoxifen-induced recombination leads to irreversible expression of the enhanced yellow fluorescent protein (eYFP) in CX₃CR1^{+} embryonic precursors and their progeny (that is, fetal monocytes and differentiated macrophages at the time of tamoxifen injection; for review see ref. [37]).

UV-induced skin injury

Mice were anaesthetized with ketamine/xylazine, shaved and depilated (Veet cream) and then left untreated or exposed to UV (λ = 254 nm; voltage 8 W; source 30 cm from the target) for 25 min. The protocol described previously[2] was adapted so that the ear skin of wild-type mice can recover in 35 days after UV exposure. Ear thickness was measured every other day with a caliper (under isoflurane anaesthesia) and compared to the ear thickness of control untreated mice.

Histology and histopathological analysis

At different times post-irradiation, mice were lethally anaesthetized using ketamine/xylazine (20 µl g^{-1}) and perfused with 10 ml PBS. Ears were then collected and fixed with formol (for at least 1 h), then cryoprotected with sucrose 30% overnight and embedded in paraffin. Skin sections (5 µm) were stained with H&E, Masson's trichrome or Picro-Sirius red. Histological scores were blindly assessed by a pathologist following the criteria described below. Leukocyte infiltration, epidermal thickness and fibrosis were evaluated and a score was assigned based on severity for each criterion. Fibrosis was also evaluated using a semi-quantitative binary score based on percentage of surface modified by fibrotic changes. A cumulative score was then obtained.

Histopathological grading

Inflammation/leukocyte infiltration. 0, no inflammation; 1, mild dermatitis (less than 10 leukocytes per high power field (HPF)); 2, moderate dermatitis (less than 50 leukocytes per HPF); 3, marked dermatitis (less than 100 leukocytes per HPF); 4, severe dermatitis (more than 100 leukocytes per HPF).

Epidermal thickness. 0, normal thickness; 1, mild hyperplasia (less than 4 cellular layers); 2, moderate hyperplasia (more than 4 cellular layers); 3, marked hyperplasia (markedly thickened, stratification and epidermal crest).

Wound healing/fibrosis. 0, no granulation tissue, no fibrosis; 1, early granulation tissue and mild fibrosis; 2, moderate fibrosis (hair follicle obliteration); 3, marked fibrosis (persistent granulation tissue/cartilage obliteration).

Fibrosis extension. 1, focal or multifocal fibrosis (less than 50% fibrosis per HPF); 2, extensive fibrosis (more than 50% fibrosis per HPF).

DRG tissue sections

After lethal anaesthesia and perfusion with 5 ml of PBS and 25 ml of 4% paraformaldehyde (PFA), C2/C3 DRG were carefully dissected from the spinal cord under a binocular lens, fixed for 1 h with 4% PFA and then cryoprotected with 30% (w/v) sucrose overnight before being included in optimal cutting temperature (OCT) compound (Tissue-Tek, Sakura) and stored at −80 °C. DRG samples were sectioned at 10–12 µm using a standard cryostat (Leica).

In situ hybridization on DRG

In situ hybridization was carried out following the protocol described in ref. [15]. In brief, RNA probes were synthesized using gene-specific PCR primers and cDNA templates from mouse DRG. The following oligonucleotides were used for the nested PCRs for probe synthesis:

Tafa4-F1: TGCTCAGAAGTTCATAGCCAAA
Tafa4-R1: TAAAGGAACATTTGCAAGCTCA
Tafa4-F2: ATATGTGCAGTGTGG
Tafa4-R2 + T7: TAATACGACTCACTATAGGGCAGCCAAGTTCAAAC

DRG sections were treated with proteinase K, triethanolamine and acetic anhydride solutions. Digoxigenin labelled probes were hybridized overnight at 55 °C after 2 h of prehybridization. The slides were treated with 0.2X SSC baths then blocked at room temperature with 10% goat serum and incubated with anti-digoxigenin antibodies (Roche). Final detection was achieved using Cyanine 3 TSA plus kit (Perkin Elmer).

Immunofluorescent and confocal analysis of DRG neuron activation

We used the expression of ATF3 as a proxy for neuronal injury and activation[38]. DRG sections were saturated and permeabilized with a PBS

1X, 3% BSA, 0.3% Triton X-100 and 10% donkey serum (Sigma, D9663-10ML) solution for 1 h at room temperature before adding the primary anti-mouse TAFA4 antibody (rat clone 1D8, 1:1,000), anti-mouse GINIP (rat, 1:1,000, from the laboratory of A.M.; IBDM, France) or anti-mouse GINIP (rabbit, 1:1,000, Invitrogen, PA5-71131), anti-mouse ATF3 (rabbit, 1:200, Santa Cruz, SC-188 or Abcam, ab207434), anti-TH (1:300, Merck Millipore, AB152) and anti-mouse CGRP (goat, 1:1,000, Abcam, ab36001) for 24 h, at 4 °C. After several washes, donkey secondary antibodies (anti-mouse, 715-585-151; anti-rat, 712-545-153; anti-rabbit, 711-585-152; and anti-goat, 705-605-147; from Jackson ImmunoResearch, 1:500) were added for 45 min at room temperature. The staining with isolectin B4 (IB4) coupled to AlexaFluor 647 (AF647; 1:200, Invitrogen) was performed in TNT buffer (Tris HCl 100 nM, NaCl 150 nM, Tween-20 0.1% pH 7.5) for 45 min at room temperature. Images were acquired using a confocal microscope (LSM780, Zeiss) and analysed using ZEN 2.3 and ImageJ Software.

Skin-cell isolation
After lethal anaesthesia and intracardiac perfusion with 5 ml of PBS, ears were collected and dorsal and ventral layer separated, finely minced with scissors in complete medium (RPMI+L-glutamine, 10% FCS) and incubated for 1 h at 37 °C with 1 mg ml^{-1} DNase (Roche) 0.2 mg ml^{-1} dispase (Gibco) and 0.2 mg ml^{-1} collagenase type IV (Sigma; C5138-500MG). Tissues were then dissociated using 2.5 ml syringes and 18G needles and filtered on a cell strainer (100 µm, BD Biosciences), washed in FACS buffer (PBS-2 mM EDTA, FCS 2%) to obtain a homogeneous cell suspension ready for staining.

Isolation of DRG neurons
After lethal anaesthesia and intracardiac perfusion with 5 ml of HBSS 10X (Mg^{2+}-free and Ca^{2+}-free), HEPES 5 mM, D-glucose 12.5 mM and penicillin/streptomycin (P/S) 1% solution, DRGs were carefully extracted and digested twice with a 0.2 mg ml^{-1} collagenase type II (Gibco) and 0.5 mg ml^{-1} dispase (Gibco) solution for 30 min at 37 °C. After several washes with Neurobasal complete medium (B-27 2%, L-glutamine 20 mM, P/S 1%), DRGs were mechanically dissociated using three needles of decreasing diameter (18G, 22G, 26G). After a filtration on a cell strainer (70 µm, Miltenyi Biotec), a Percoll gradient was used with 12.8% and 28% density in Leibovitz-15 complete medium (FCS 5% and P/S 1%) to eliminate cell debris. After centrifugation and several washes, the cell suspension was ready for staining.

Antibodies for flow cytometry
We adapted our FACS gating strategy from previous studies[39], adding EpCAM, Langerin (CD207) or CD206 and TIM4 to decipher the monocyte/macrophage compartment of the skin. Antibodies were purchased from BioLegend or BD Biosciences: CD45-BV785 1:500 (30F11), CD45.1-BV605 1:200 (A20), CD11b-BV510 1:1,000 (M1/70), CD64-BV711 1:300 (X54-5/7.1), Ly6C-421 1:300 (AL-21), F4/80-PECF594 1:400 (T45-2342), CD11c-BUV395 1:200 (N418), EpCAM-AF594 1:500 (G8.8), CD207-APC 1:200 (929F3.01; Dendritics, DDX0362), CD206-APC 1:300 (C068C2), TIM4-PeCy7 1:300 (RMT4-54) Ly6G-APC-Cy7 1:300 (1A8), IA-IE A700 1:500 (M5/114.15.2), CD24-BUV737 1:500 (M1/69). Mast cells were characterized as previously described[40,41], CD117-BV605 (Kit; 2B8; 1:300), CD103-PerCP-Cy5.5 (2E7; 1:500), anti-TNF-PE 1:100 (MP6-XT22) anti-IL-10-PE 1:100 (JES5-16E3); CCR2-PE 1:200 (475301; R&D System), IL-1β-PE 1:100 (NJTEN3; eBioscience), anti-CD4 PE-Cy7 (RM4-5; BD), anti-TCRαβ APC-Cy7 (H57-597; BD), anti-FoxP3-A488 1:200 (Clone FJK-16 s; eBioscience), anti-DTR 1:300 (anti-hHB-EGF; AF-259-NA; R&D System), anti-GFP (Invitrogen, A-21311).

Flow cytometry
Cell suspensions were plated in 96-well U bottom plates and stained at 4 °C. Cells were incubated for 40 min at 4 °C in FACS buffer with antibodies and anti-Fc receptor blocking antibody (clone: 2.4 G2). Cells were then washed and fixed (fixation buffer, from FoxP3 kit; eBioscience; 00-5521-00) until analysis. For intracellular cytokine staining, cell suspensions were permeabilized (Fix/perm, from FoxP3 kit; eBioscience) and stained with anti-cytokine antibodies for 1 h for IL-1β and TNF or overnight for IL-10. For IL-10 expression analysis in FoxP3$^+$ T$_{reg}$ cells, total skin homogenates were incubated for 6 h in complete medium supplemented with PMA (200 ng ml^{-1}; Sigma) and ionomycin (1 mg ml^{-1}; Sigma). During the last 4 h, Golgi Plug (1:1,000; BD Biosciences; 554724) was added. Cell suspensions were then washed extensively at 4 °C, surface-stained, fixed and then processed for intracellular staining. Dead cells were excluded from the analysis by counter-gating using the live/dead fixable blue Dead Cell Stain kit UV (L23105; Invitrogen). Multiparameter FACS analysis was performed using an LSR X20 system (BD Biosciences). Absolute numbers for each population were obtained using Quanti Beads (BD Biosciences, 556296). Data analysis was performed using FlowJo software (Tree Star).

t-Distributed stochastic neighbour embedding
t-SNE analyses were performed using FlowJo v.10 software (FlowJo LLC). We used an equal number of mice for each genotype or experimental condition considered. In each group, the same number of cells was used to allow an equivalent contribution of each individual mice in the analysis. This equal cell number was selected using the DownSample plugin. Then, cells from each mouse were merged using the concatenate tool and barcoded to track and distinguish them. Finally, t-SNE analyses were performed using different markers, indicated in the figure legends. The colour code representing the expression level of each marker in the heat maps (depicted in Extended Data Figs. 4b, 8g), is normalized on the median intensity value for a given marker. Data are represented using a four-colour scale with blue, green–yellow and red indicating low, intermediate and high expression levels, respectively (see expression level scales provided).

Immunofluorescent staining and confocal microscopy analysis of ear skin
After lethal anaesthesia and perfusion with 10 ml PBS, ears from diphtheria-toxin-treated GINIP-DTR and DTR control mice were collected and ear dorsal and ventral layers were separated, fixed for 1 h with 4% PFA, washed, permeabilized and saturated with PBS, 3% BSA, 0.2% Triton X-100 and 10% donkey serum and then stained with primary anti-mouse GINIP antibody (rat, 1:300; A.M. laboratory, IBDM, France) and anti-TH antibody (rabbit, 1:300; Merck Millipore, AB152) overnight at 4 °C. After several washes, a donkey secondary anti-rat-488 and anti-rabbit-AF594 antibody (Jackson Immunoresearch, 1:500) were added for 1 h at room temperature, washed, and then the anti-beta III tubulin-AF647 antibody (1:300 TUJI; BioLegend, BLE801210) or the anti-CD206-APC 1:300 (rat, 1:300; clone C068C2, BioLegend, BLE141708), were added for an additional 45 min at room temperature. After several washes, slices were then mounted on coverslips with mounting medium and image acquisition was performed on Confocal LSM780 (Zeiss) and analysed with ZEN and ImageJ software.

BMDM generation
Femora bones were isolated from wild-type or Fpr1-knockout mice (bone marrow cells from Fpr1-knockout mice were provided by M. Lucattelli and L. Zitvogel), cut in half and placed in 0.5 ml Eppendorf tubes pre-perforated on their bottom part. These small tubes containing two halves of a bone were placed within 1.5 ml Eppendorf tubes. The tubes were then centrifuged for 10 s at 16,000g and bone marrow cell pellets were resuspended in red blood cell lysis buffer for 3 min and washed in PBS. Bone marrow cells were then resuspended at 10^6 per ml in complete DMEM (DMEM, SVF 10%, P/S, 1% L-Glu) supplemented with 20% conditioned L929 medium for 5 days to generate BMDMs and used as thioglycollate-elicited macrophages for in vitro experiments.

Article

Thioglycollate-elicited macrophage generation and in vitro treatment

Peritoneal macrophages were isolated from wild-type mice by peritoneal wash three days after i.p. injection of 3% thioglycollate (Sigma). Peritoneal washes were then stained with biotin-associated lineage cocktail antibodies (CD3, CD19, NK1.1, Ly6G and Siglec F), counterstained with anti-biotin microbeads (Miltenyi Biotec) and then purified using magnetic LS columns. Peritoneal macrophage preparations were then cultured in complete DMEM (DMEM, SVF 10%, P/S, 1% L-Glu) at 10^6 thioglycollate-elicited macrophages per ml in a 12-well plates (BD) with or without LPS (100 ng ml^{-1}, Sigma) in the presence or absence of 100 nM TAFA4. After 16 h, macrophages were lysed using RLT medium (Qiagen) then passed through a QIAShredder column (Qiagen) and stored at −80 °C.

Migration assay

BMDM from wild-type or *Fpr1*-knockout mice were incubated on the top chambers of transwell plates (Costar) in complete DMEM, while the bottom chambers of the transwell plates were filled with complete DMEM for negative control, or complete DMEM containing CCL2 (MCP-1; 10 nM) for positive control of migration, or increasing concentrations of TAFA4 (1–1,000 nM), for 8 h at 37 °C. The bottom chambers were then analysed by FACS for macrophage content.

Dermal resident macrophage depletion

Wild-type or *Tafa4*-knockout mice were injected on two consecutive days with 500 µg of the CSF-1R blocking antibody (clone AFS98; InVivoMAb, BioXcell, BE0213) or the isotype control (IgG2a; clone 2A3; InVivoMAb, BioXcell, BE0089). One day after the last injection, mouse tissues were collected and analysed for macrophage depletion by flow cytometry.

Dermal resident macrophage isolation

Ear skin from wild-type or *Tafa4*-knockout mice was dissociated and stained as previously described, and CD206$^+$ dermal resident macrophages were sorted on a FACS Aria III following the gating strategy in Extended Data Figs. 3a, 4a as livedead$^-$, CD45$^+$DC$^-$CD11b$^+$CD24$^-$Ly6G$^-$CR2$^-$Ly6C$^-$CD64$^+$CD206$^+$, then lysed using RLT medium (Qiagen) then passed through a QIAShredder column (Qiagen) and stored at −80 °C. Alternatively, TIM4$^+$ macrophages or inflammatory macrophages (CD64$^+$CD206$^-$) were sorted as presented in Extended Data Fig. 10b.

Intradermal adoptive transfer of inflammatory and TIM4$^+$ macrophages

DTR and GINIP-DTR mice were exposed to UV and then intradermally injected at D1 post-irradiation with 2,000 macrophages per 10 µl PBS per ear.

Imiquimod-induced cutaneous damage

Wild-type or *Tafa4*-knockout mice were treated daily with 5 mg of 5% imiquimod cream applied topically to dorsal and ventral aspects of the ear skin as previously described[6] for six days, and the change in ear thickness (µm) was followed every day with a caliper.

TAFA4 rescue and in vivo blocking of IL-10

For TAFA4 rescue experiments, 20 µl of either recombinant TAFA4 (25 µg ml^{-1}) or saline solution were intradermally injected every other day following the UV-treatment until day 8 post-irradiation in each ear of *Tafa4*-knockout or control mice as indicated in Fig. 4g.

For IL-10 blocking experiments, 20 µl of anti-IL-10 blocking antibody (0.5 mg ml^{-1}; R&D, MAB417) or the isotype control (rat IgG1; clone JES052A5) were intradermally injected every other day following the UV-treatment until day 8 post-irradiation in each ear of *Tafa4*-knockout or control mice as indicated in Extended Data Fig. 9a.

Gene expression analysis

Total RNA was isolated from mouse ears, exposed or unexposed to UV irradiation, or from BMDM or thioglycollate-elicited macrophages activated with or without LPS and TAFA4. Ears were dilacerated by FastPrep-24 (MpBio) in lysis matrix A tubes (MpBio). RNA was isolated using a fibrous RNeasy mini kit (Qiagen). Reverse transcription was performed using Superscript RTII (Invitrogen). Pre-amplification was performed using specific Taqman probes (Applied Biosystems) for each targeted gene using the pre-amplification master mix (Fluidigm). Pre-amplified products (18 cycles) were diluted (1:5) in Universal PCR Master Mix then loaded in a 96.96 Dynamic Array and analysed on a BioMark Genetic Analysis System (Fluidigm). Data were normalized ($2^{-\Delta Ct}$) to the housekeeping genes, *Gapdh* and *Hprt*.

Primers used for mRNA detection in total skin samples (TaqMan references)

Acta2 (Mn00808218_g1); *Areg* (Mm00437583_m1); *Ccl1* (Mm00441236_m1); *Ccl2* (Mm00441242_m1); *Ccl3* (Mm00441259_g1); *Clc4* (Mm00443111_m1); *Clc6* (Mm01302419_m1); *Ccl8* (Mm01297183_m1); *Cd36* (Mm00432403_m1); *Cebpb/d* (Mm00786711_s1); *Chil3* (Mm00657889_mH); *Col1a1* (Mm00801666_g1); *Col3a1* (Mm00802305_g1); *Cxcl2* (Mm00436450_m1); *Cxcl9* (Mm00434946_m1); *Cxcl10* (Mm00445235_m1); *Des* (Mm00802455_m1); *Egr1* (Mm00656724_m1); *Epas* (Mm01236112_m1); *Fam19a4* (*Tafa4*, Mm00623620_m1); *Flt3* (Mm00439016_m1); *Gf1r* (Mm00616224_m1); *Ifnb1* (Mm00439552_s1); *Il1b* (Mm00434228_m1); *Il1r1* (Mm00434237_m1); *Il4* (Mm00445259_m1); *Il12a* (Mm00434169_m1); *Il13* (Mm00434204_m1); *Il15* (Mm00434210_m1); *Il17a* (Mm00439618_m1); *Il22* (Mm01226722_g1); *Il23a* (Mm00518984_m1); *Irf3* (Mm01203177_m1); *Irf7* (Mm00516791_g1); *Irf8* (Mm00492567_m1); *Klf2* (Mm00500486_g1); *Klf4* (Mm00516104_m1); *Klf5* (Mm00456521_m1); *Mmp2* (Mm00439498_m1); *Mmp9* (Mm00442991_m1); *Mmp10* (Mm01168399_m1); *Mmp12* (Mm00500554_m1); *Mpo* (Mm00447885_m1); *Mtor* (Mm00444968_m); *Nos2* (Mm00440502_m1); *Nr4a1* (Mm01300401_m1); *Nr4a3* (Mm00450071_g1); *Pdgfra* (Mm00440701_m1); *Pdgfrb* (Mm01262485_m1); *Piezo1* (Mm01241544_g1); *Piezo2* (Mm01262422_g1); *Plod2* (Mm00478767_m1); *Pparg* (Mm00440940_m1); *Retnla* (Mm00445109_m1); *Ripk1* (Mm00436360_m1); *Serpinb9* (Mm00777163_m1); *Tac1* (Mm01166994_g1); *Tgfbr2* (Mm03024091_m1); *Tlr3* (Mm01207402_m1); *Tlr4* (Mm00445273_m1); *Tlr7* (Mm04933178_g1); *Tlr9* (Mm07299609_m1); *Trp53* (Rn00755717_m1); *Gapdh* (Mm99999915_g1); *Hprt* (Mm03024075_m1).

Protein extraction from tissue

Mice were euthanized and their ears were snap-frozen in liquid nitrogen and then transferred into mechanical dissociation tubes (Lysis Matrix A, MPbio) containing a commercial lysis buffer (T-Per Tissue Protein Extraction Reagent, Thermo Fisher) with protease inhibitor cocktail (Halt Protease Inhibitor 100X, Thermo Fisher). Protein extraction was performed by incubating each gram of tissue with 20 ml of lysis buffer. Tissues were dissociated using a 3-cycle program of FastPrep-24 5G (MP Bio). After two centrifugations at 16,000*g* for 30 min, the supernatants were filtered (on 70-µm cell strainers, Startedt) and stored at −80 °C until use.

Generation of recombinant mouse TAFA4

Mouse TAFA4 recombinant protein was produced in *E. coli* by Pure Biologics (https://purebiologics.pl). The endotoxin levels of the purified protein, measured by the Limulus Amoebocyte Lysate method, was <0.0005 EU µg^{-1}. The recombinant protein included a histidine (His)-tag in the C-terminal part of the protein, enabling its detection by anti-His antibodies. The sequence of this recombinant mTAFA4 is:

MHLIKPGTCEVVAVHRCCNKNRIEERSQTVKCSCFPGQVAGTTRAQPS CVEAAIV

IEKWWCHMNPCLEGEDCKVLPDSSGWSCSSGNKVKTTKVTRGGGSGL EHHHHHH

Generation of anti-TAFA4 monoclonal antibodies

Anti-TAFA4 monoclonal antibodies (mAbs) were generated by MImAbs (https://www.mimabs.org). In brief, three Wistar rats were immunized with the recombinant mouse TAFA4 protein (100 µg, 3 i.p. injections followed by a final boost). After immunization, spleen cells were collected and fused to the myeloma cell line X63-Ag8-656. Hybridoma were seeded in methylcellulose semi-solid medium with CloneDetect agent (Molecular Devices, K8240) and secreting monoclonal IgG hybridomas were picked by ClonePix2 (Molecular Devices) to liquid medium 96-well plates. Hybridoma clones producing anti-TAFA4 antibodies were selected using an ELISA screen. The specificity of the antibodies for the native TAFA4 protein was assessed by immunofluorescent staining on mouse DRG from wild-type (positive control) or *Tafa4*-knockout (negative control) mice.

Sandwich ELISA for TAFA4 quantification

To quantify TAFA4 protein, a sandwich enzyme-linked immunosorbent assay (ELISA) has been developed by MImAbs. In brief, anti-TAFA4 antibodies (clone 33F8, 50 µl, 2 µg ml^{-1}) diluted in an Na_2CO_3/$NaHCO_3$ buffer (Sigma, C3041-100CAP, pH 9.6) were coated on 96-well MAXISORP plates (Sigma, M5785-1CS) and incubated overnight at 4 °C. Plates were then washed three times in a washing buffer (PBS/0.1% Tween-20) and blocked with 300 µl of StartingBlock blocking buffer (Thermo Fisher, 37542). Samples and serial dilutions of mTAFA4 (to establish the standard curve) were incubated for 1 h 30 min at room temperature. After three washes, anti-TAFA4 biotinylated antibodies (clone 1D8, 50 µl, 1 µg ml^{-1}) were incubated for 1 h 30 min at room temperature. After three washes, HRP-conjugated streptavidin (Thermo Fisher, N100) was added, with three further washes before adding the substrate solution TMB (Interchim, UP664781). After 10 additional minutes, the reaction was stopped with a solution of HCl (1 M) and the absorbances (at 450 nm and 620 nm) of each well were measured. The specific signal obtained for wild-type ear skin samples was determined by subtracting the background signal obtained with skin samples from *Tafa4*-knockout mice.

Cytokine and chemokine quantification in skin samples

Ear skin samples were homogenized and protein extraction was performed as described in the section 'Protein extraction from tissue'. Cytometric bead array (CBA) Flex Set kit (BD Biosciences) was used to quantify chemokine ligand 1 (CXCL1), tumour necrosis factor (TNF), interleukin 6 (IL-6), interleukin 1 beta (IL-1β), monocyte chemoattractant protein 1 (CCL2, also known as MCP1) and the chemokine (C−C motif) ligands 4 (CCL4). For IL-10, an enhanced sensitivity CBA Flex Set kit (BD Bioscience) was used. Samples were analysed on a Canto II flow cytometer with FCAP Array TM Software (BD Biosciences) following manufacturer's instructions.

Statistical analysis

All results are expressed as mean ± s.e.m. Statistical analyses were performed using GraphPad Prism for Windows. Statistical analysis was performed using a one-way ANOVA with Tukey's multiple comparisons test throughout the study. A two-way ANOVA test was used to compare two or more than two groups in kinetic experiments after UV exposure, involving repeated measures on the same mice over time. Difference were considered significant as follows: *$P < 0.05$; **$P < 0.01$; ***$P < 0.001$; ****$P < 0.0001$.

Reporting summary

Further information on research design is available in the Nature Research Reporting Summary linked to this paper.

Data availability

All data supporting the findings of this study are found within the manuscript and its Supplementary Information, and are available from the corresponding author upon reasonable request. Source data are provided with this paper.

34. Madan, R. et al. Nonredundant roles for B cell-derived IL-10 in immune counter-regulation. *J. Immunol.* **183**, 2312–2320 (2009).
35. Reber, L. L. et al. Imaging protective mast cells in living mice during severe contact hypersensitivity. *JCI Insight* **2**, e92900 (2017).
36. Misharin, A. V. et al. Monocyte-derived alveolar macrophages drive lung fibrosis and persist in the lung over the life span. *J. Exp. Med.* **214**, 2387–2404 (2017).
37. Hoeffel, G. & Ginhoux, F. Ontogeny of tissue-resident macrophages. *Front. Immunol.* **6**, 486 (2015).
38. Renthal, W. et al. Transcriptional reprogramming of distinct peripheral sensory neuron subtypes after axonal injury. *Neuron* **108**, 128–144.e9 (2020).
39. Tamoutounour, S. et al. Origins and functional specialization of macrophages and of conventional and monocyte-derived dendritic cells in mouse skin. *Immunity* **39**, 925–938 (2013).
40. Gentek, R. et al. Hemogenic endothelial fate mapping reveals dual developmental origin of mast cells. *Immunity* **48**, 1160–1171.e5 (2018).
41. Serhan, N. et al. House dust mites activate nociceptor-mast cell clusters to drive type 2 skin inflammation. *Nat. Immunol.* **20**, 1435–1443 (2019).

Identification of DRGs innervating the ear skin by DiI retrolabeling
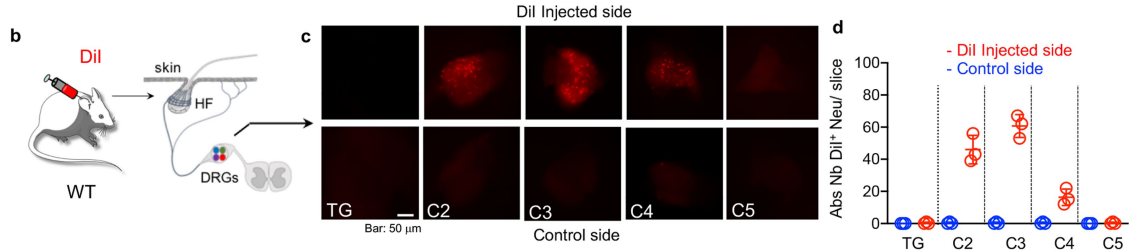
UV exposure selectively activate GINIP⁺ neurons in C2/C3 DRGs
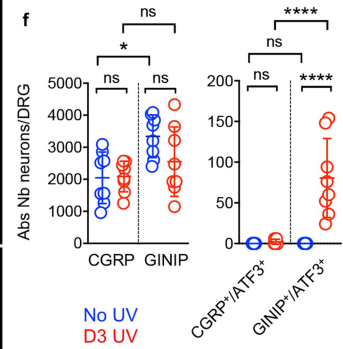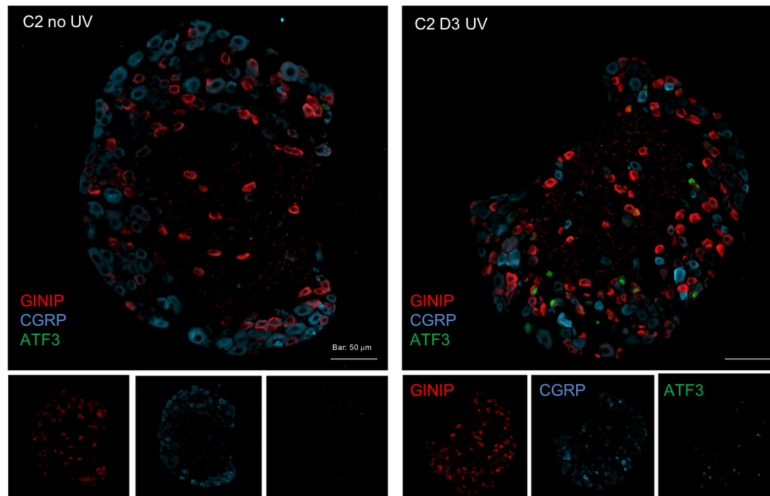
Extended Data Fig. 1 | See next page for caption.

Extended Data Fig. 1 | UV overexposure triggers a sequence of skin inflammation and repair over 35 days and GINIP⁺ neuron activation. a, Heat map representing the expression kinetics of genes involved in skin inflammation and repair over time (days) post-irradiation. Ears from wild-type mice were collected before UV irradiation (day (D)0) or at D3, D7, D14 and D35 post-irradiation and total extracted RNA was analysed by Fluidigm. Genes encoding proinflammatory cytokines and chemokines were expressed at D3 and D7 delineating the inflammatory phase (red cluster). Pro-repair genes were upregulated at D14 and D35 (green cluster) delineating the resolution/ remodelling phases. The gene *Fam19a4* (also known as *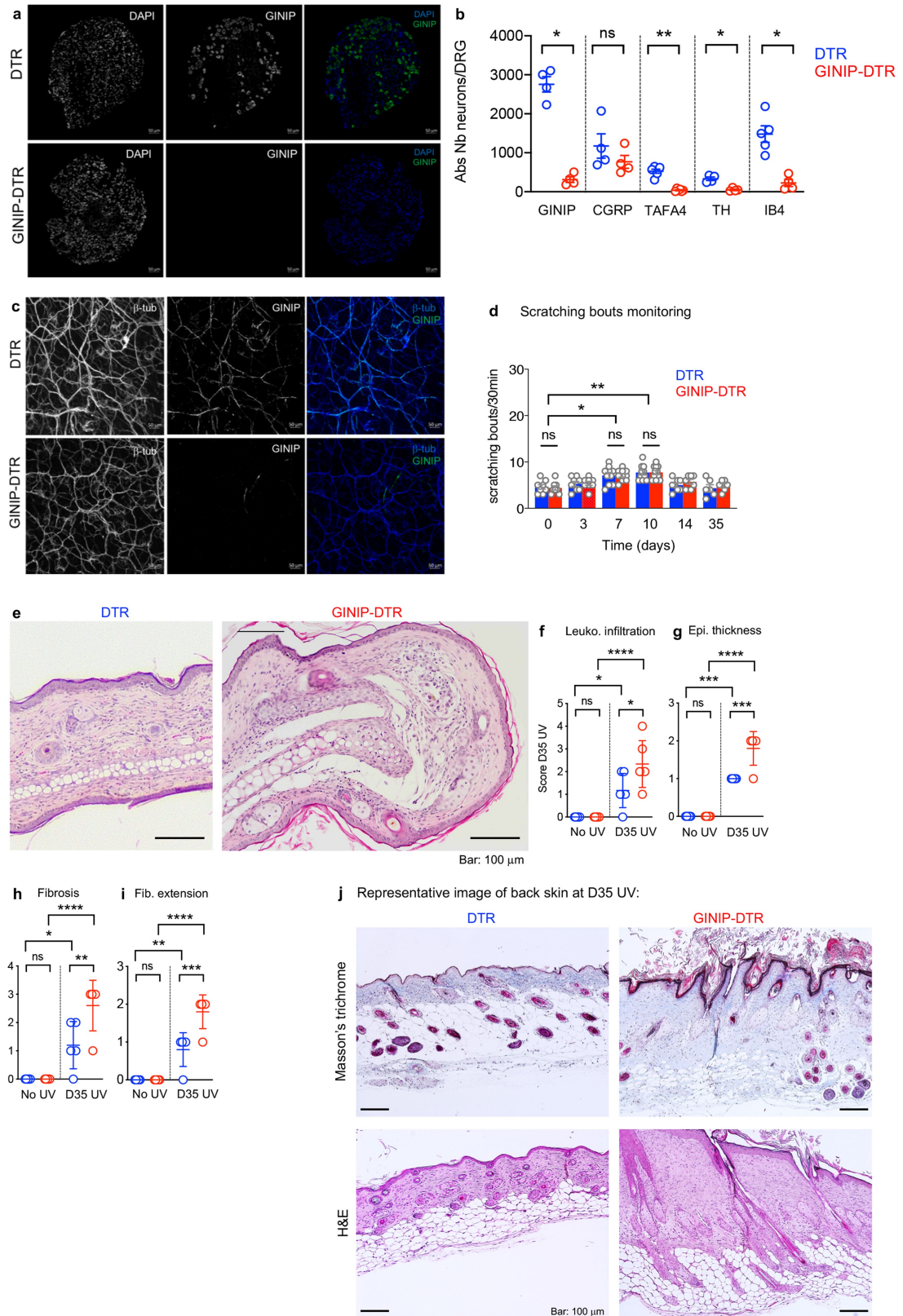Tafa4*) that encodes TAFA4 is highlighted in yellow (*n* = 4–8 mice per group). **b**, Sensory neurons from C2/C3 DRGs innervate the ear skin. The fluorescent tracer DiI was injected intradermally in the right ears of wild-type mice and the left ears were injected with PBS (*n* = 3 independent DRGs per group). **c**, The trigeminal ganglia (TG) and cervical DRG (C2 to C5) were collected 48 h post-injection and analysed by fluorescent microscopy. **d**, Quantification of DiI⁺ neurons per DRG fields of view; PBS-injected control side (blue) or DiI-injected side (red). **e**, Additional representative confocal images (related to Fig. 1c) of C2 DRGs labelled for GINIP (red), CGRP (blue) and ATF3 (green), from unexposed (left) and UV-exposed (right) mice at D3 post-irradiation. **f**, Quantification of total GINIP⁺ and CGRP⁺ neurons per DRGs (left) and total CGRP⁺ATF3⁺ and GINIP⁺ATF3⁺ DRG neurons (right) from unexposed (blue) and UV-exposed (red) mice at D3 post-irradiation (*n* = 8 mice per group). All data are representative of at least two independent experiments and presented as mean ± s.e.m. *P* values determined by one-way ANOVA with Tukey's multiple comparisons test. NS, not significant; *$P < 0.05$; **$P < 0.01$; ***$P < 0.001$.

a

DTR: DAPI | GINIP | DAPI GINIP

GINIP-DTR: DAPI | GINIP | DAPI GINIP

b

Abs Nb neurons/DRG

* (GINIP), ns (CGRP), ** (TAFA4), * (TH), * (IB4)

DTR (blue), GINIP-DTR (red)

c

DTR: β-tub | GINIP | β-tub GINIP

GINIP-DTR: β-tub | GINIP | β-tub GINIP

d Scratching bouts monitoring

scratching bouts/30min

DTR (blue), GINIP-DTR (red)

ns, *, **, ns, ns

Time (days): 0, 3, 7, 10, 14, 35

e

DTR | GINIP-DTR

Bar: 100 μm

f Leuko. infiltration

Score D35 UV

ns, *, *, ****

No UV | D35 UV

g Epi. thickness

ns, ***, ***, ****

No UV | D35 UV

h Fibrosis

ns, *, **, ****

No UV | D35 UV

i Fib. extension

ns, **, ***, ****

No UV | D35 UV

j Representative image of back skin at D35 UV:

DTR | GINIP-DTR
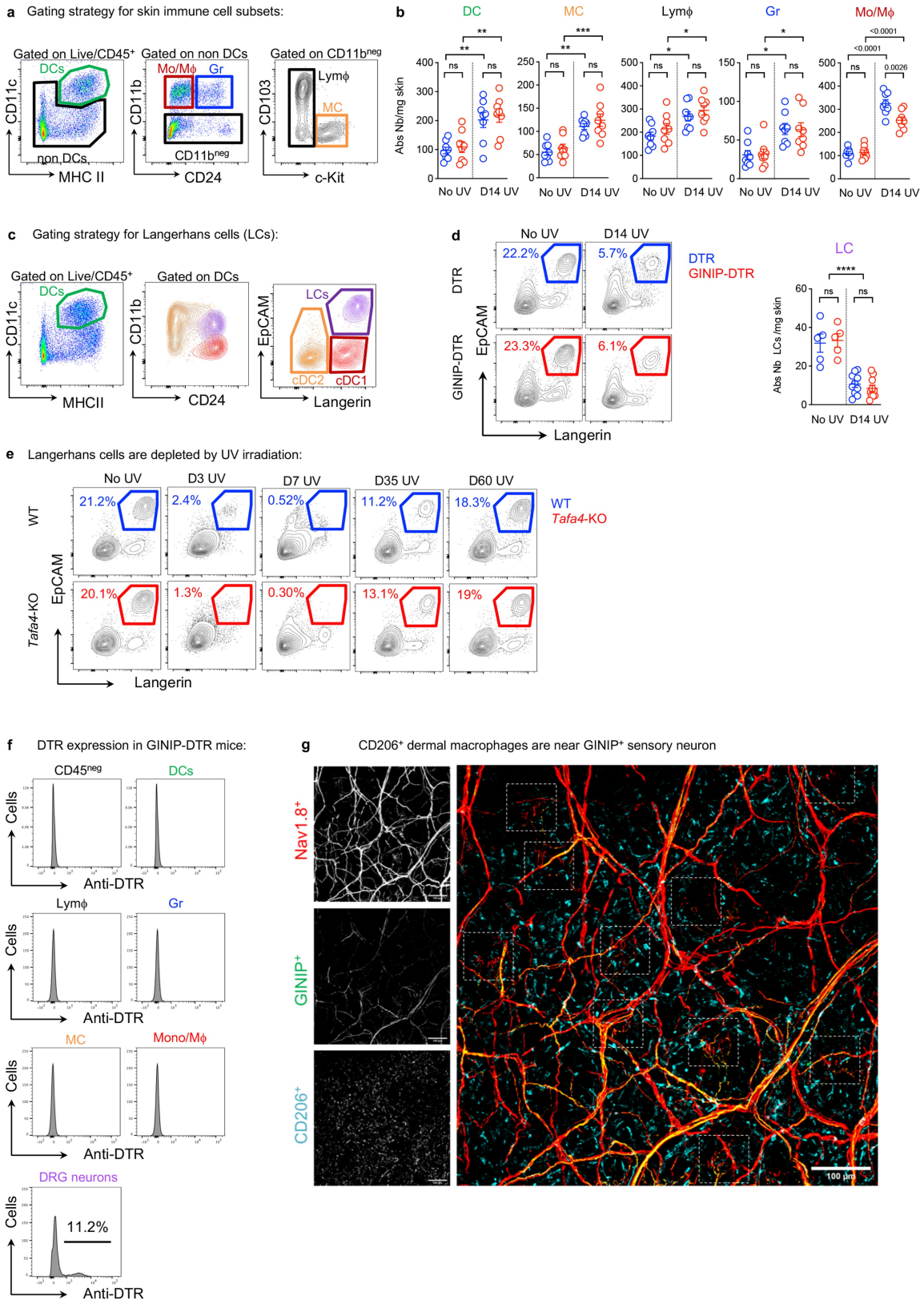
Masson's trichrome

H&E

Bar: 100 μm

Extended Data Fig. 2 | See next page for caption.

Extended Data Fig. 2 | Conditional ablation of GINIP⁺ neurons in GINIP–DTR mice and skin histopathological analysis after UV exposure. a, Representative confocal images for DAPI (blue) and GINIP (green) staining of C3 DRGs from control DTR-control (top) and GINIP-DTR (bottom) mice, 10 weeks after diphtheria toxin (DT)-treatment. **b**, Absolute number of GINIP⁺, CGRP⁺, TAFA4⁺, TH⁺ and IB4⁺ DRG neurons were quantified in DTR-control (blue) and GINIP-DTR (red) mice (n = 4–6 independent DRG per group). **c**, Representative confocal images for Beta3-tubulin (blue) and GINIP (green) staining of mouse ear skin sections as in **a**. **d**, Scratching episodes were monitored for 30 min at each time point post-irradiation indicated (n = 6–10 mice per group). **e**, Representative H&E staining of ears from DTR (left) and GINIP-DTR (right) mice at D35 post-irradiation. **f–i**, Histopathological analysis for leukocyte infiltration (**f**), epidermal thickness (**g**), fibrosis (**h**) and fibrosis extension (**i**) (n = 5 mice per group); related to Fig. 1g–j. Criteria used for the histopathological scoring are described in the Methods. **j**, Representative Masson trichrome (top) and H&E staining (bottom) of back skin from DTR-control (left) and GINIP-DTR (right) mice at D35 post-irradiation. All data are representative of at least two independent experiments and presented as mean ± s.e.m. P values determined by one-way ANOVA with Tukey's multiple comparisons test. NS, not significant; *P < 0.05; **P < 0.01; ***P < 0.001.

a Gating strategy for skin immune cell subsets:

b

c Gating strategy for Langerhans cells (LCs):

d

e Langerhans cells are depleted by UV irradiation:

f DTR expression in GINIP-DTR mice:

g CD206+ dermal macrophages are near GINIP+ sensory neuron

Extended Data Fig. 3 | See next page for caption.

Extended Data Fig. 3 | Immune cell subsets in the skin before and after UV exposure. a, Flow cytometry gating strategy using CD11b, CD11c, CD64, MHC-II, CD103, c-Kit, Ly6G and CD24 marker expression. Dendritic cells (DC; CD11c$^+$ MHC-II$^+$), mast cells (MC; CD11b$^-$Kit$^+$), lymphoid cells (Lymφ; CD11b$^-$CD103$^{-/+}$), granulocytes (CD11b$^+$CD24$^+$, Ly6G$^+$) and the monocyte/macrophage compartment (Mo/Mφ; CD11c$^-$MHC-II$^-$CD11b$^+$CD24$^-$Ly6G$^-$CD64$^{int/+}$) are shown. **b**, Absolute numbers per mg of skin for dendritic cells, MC, Lymφ, Gr and monocyte/macrophage populations at D14 post-irradiation in DTR-control (blue) or GINIP-DTR (red) mice (n = 8 mice per group). **c**, Gating strategy for skin dendritic cell subsets (CD11c$^+$MHC-II$^+$) and monitoring of Langerhans cells (LC; EpCAM$^+$Langerin$^+$) (n = 5–8 mice per group). **d**, FACS plot for Langerhans cells (left) and quantification (right) in DTR-control and GINIP-DTR mice, unexposed (no UV) or at D14 post-irradiation (UV) (n = 5–10 mice per group). **e**, Percentage of Langerhans cells among dendritic cells over time post-UV exposure in wild-type and *Tafa4*-knockout mice. **f**, Representative flow cytometry analysis of skin immune cells and DRG neurons for the expression of DTR in GINIP–DTR mice. **g**, Confocal analysis of whole mount ear skin from *Nav1.8-RFP* mice stained for GINIP$^+$ neurons and CD206$^+$ dermal resident macrophages. Hair follicles (HF) are highlighted within white dashed squares. In the skin, Na$_v$1.8 expression (RFP) is restricted to sensory neuron axonal extensions. In DRG (**f**), DTR expression is restricted to neuronal cellular bodies in DRGs. These markers were not detected in immune cells. All data are representative of at least two independent experiments and presented as mean ± s.e.m. *P* values determined by one-way ANOVA with Tukey's multiple comparisons test. NS, not significant; *P < 0.05; **P < 0.01; ***P < 0.001.
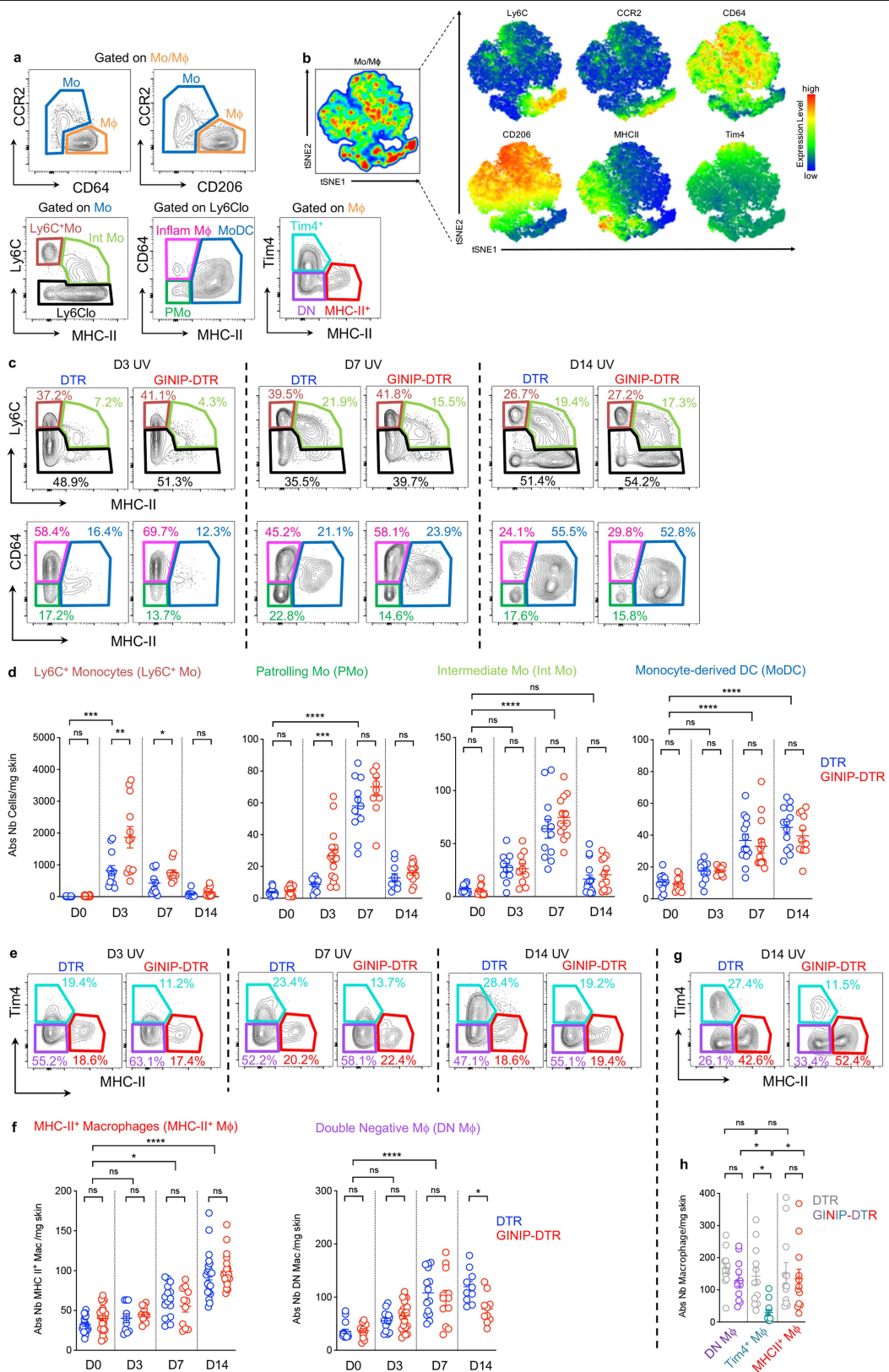
Extended Data Fig. 4 | See next page for caption.

Extended Data Fig. 4 | Flow cytometry and *t*-SNE analysis of skin monocyte/ macrophage subsets in GINIP-DTR mice. a, Classical flow cytometry gating strategy for monocyte and macrophage subsets in the skin. **b**, *t*-SNE analysis including CCR2, Ly6C, MHC-II, CD64, CD206 and TIM4 markers was performed to cluster monocyte/macrophage populations at day 14 post-irradiation in the skin of GINIP-DTR and DTR-control mice (see also Methods for *t*-SNE analysis). **c**, Representative plots for CCR2$^{-/+}$CD206^{-} monocyte subsets on D3, D7 and D14 post-irradiation in the skin of control (DTR) or GINIP-DTR mice. **d**, Absolute numbers of Ly6C^{+} monocytes, intermediate monocytes, patrolling monocytes and monocyte-derived dendritic cell subsets per mg of ear skin (n = 9–13 mice per group) as in **c**. **e**, Representative FACS plots for CD206^{+} dermal resident macrophages as in **c**. **f**, Absolute numbers of DN and MHC-II^{+} macrophage subsets per mg of ear skin (n = 9–13 mice per group) as in **c**. **g**, Representative FACS plots for CD206^{+} dermal resident macrophage subsets at D14 post-irradiation in back skin from control (DTR) or GINIP-DTR mice. **h**, Absolute numbers of macrophage subsets per mg of back skin (n = 12 mice per group) from DTR-control (grey) or GINIP-DTR (coloured) mice, at D14 post-irradiation. All data are representative of at least two independent experiments and presented as mean ± s.e.m. *P* values determined by one-way ANOVA with Tukey's multiple comparisons test. NS, not significant; *P < 0.05; **P < 0.01; ***P < 0.001.

a GINIP⁺ neurons innervate hair follicles

b GINIP⁺ neurons include TH⁺ C-LTMR

c

d WT | Tafa4-KO

e C3 no UV | C3 D3 UV

50 μm

TAFA4 IB4 ATF3

f

g WT | Tafa4 KO

h DRG

i Tissues

j Cells

k DRG
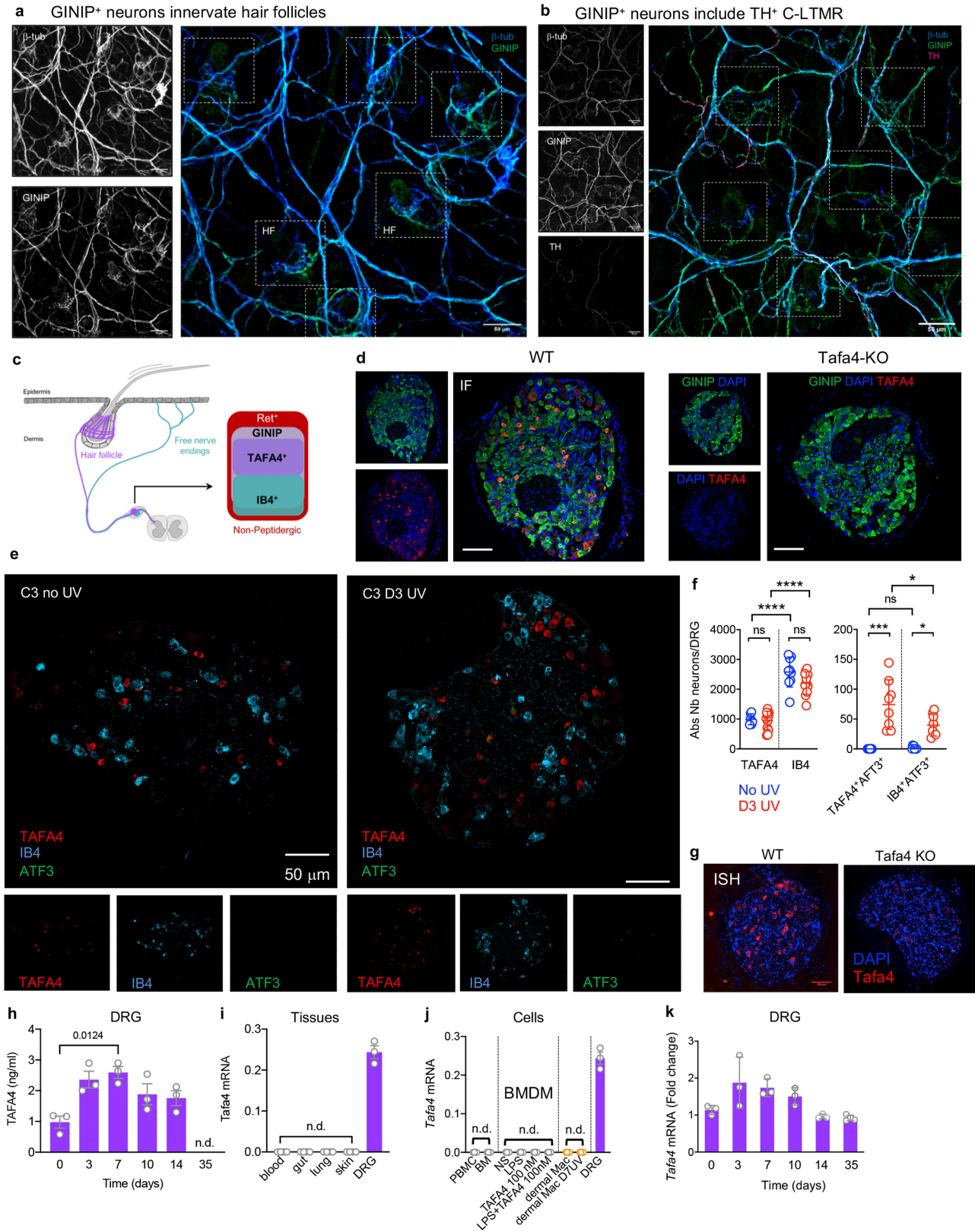
Extended Data Fig. 5 | See next page for caption.

Extended Data Fig. 5 | GINIP⁺ sensory neurons innervate hair follicles and release TAFA4 in the skin. a, Representative confocal images of whole mount ear skin from wild-type mice stained with an anti-Beta3-tubulin (blue) and anti-GINIP (green) antibodies. GINIP⁺ lanceolate barrel structures innervating hair follicles (HF) are highlighted within dashed squares. **b**, Confocal analysis as in **a** with an additional anti-TH antibody staining (red) shows GINIP⁺TH⁺ C-LTMR axon terminals reaching the hair follicle. **c**, Schematically, GINIP⁺ neurons consist of two subsets of sensory neurons projecting in the inter-follicular regions of the epidermis as free nerve endings (IB4⁺) and hair follicles as C-LTMRs (TAFA4⁺). **d**, Confocal images of DRG sections from control wild-type (left) or *Tafa4*-knockout (right) mice after immunofluorescent (IF) staining with an anti-GINIP antibody (green) and an anti-TAFA4 antibody (1D8; red) and DAPI (blue). **e**, Additional confocal images of C3 DRGs (IF) stained with IB4 (blue), anti-TAFA4 (1D8, red) and anti-ATF3 (green) antibodies in wild-type mice (related to Fig. 3a), unexposed (left) or at D3 post-irradiation (right). **f**, Absolute number of TAFA4⁺ and IB4⁺ neurons (left; $n = 6–12$ mice per group) and absolute number of TAFA4⁺ATF3⁺ and IB4⁺ATF3⁺ neurons per DRG (right) from unexposed (blue) and exposed D3 post-irradiation (red) wild-type mice, ($n = 8$ mice per group). **g**, DAPI staining (blue) in situ hybridization (ISH) for *Tafa4* mRNA (red) in DRG as in **d**. **h**, Quantification of TAFA4 levels (determined by ELISA) in DRGs from wild-type mice unexposed (D0) to D14 post-irradiation ($n = 3$ mice per time point; n.d., not determined). **i**, *Tafa4* mRNA expression (RT–qPCR) in peripheral tissues and DRGs ($n = 3$ mice per time point; n.d., not detected). **j**, Quantification of *Tafa4* mRNA expression in peripheral blood mononuclear cells (PBMCs), bone marrow, BMDMs and sorted CD206⁺ dermal macrophages compared to DRGs ($n = 3$ independent samples; n.d., not detected). **k**, *Tafa4* mRNA expression in C3 DRGs from D0 to D35 post-irradiation ($n = 3$ mice per time point). All data are representative of at least two independent experiments and presented as mean ± s.e.m. *P* values determined by one-way ANOVA with Tukey's multiple comparisons test except **h**, Kruskal–Wallis. NS, not significant; *$P < 0.05$; **$P < 0.01$; ***$P < 0.001$.
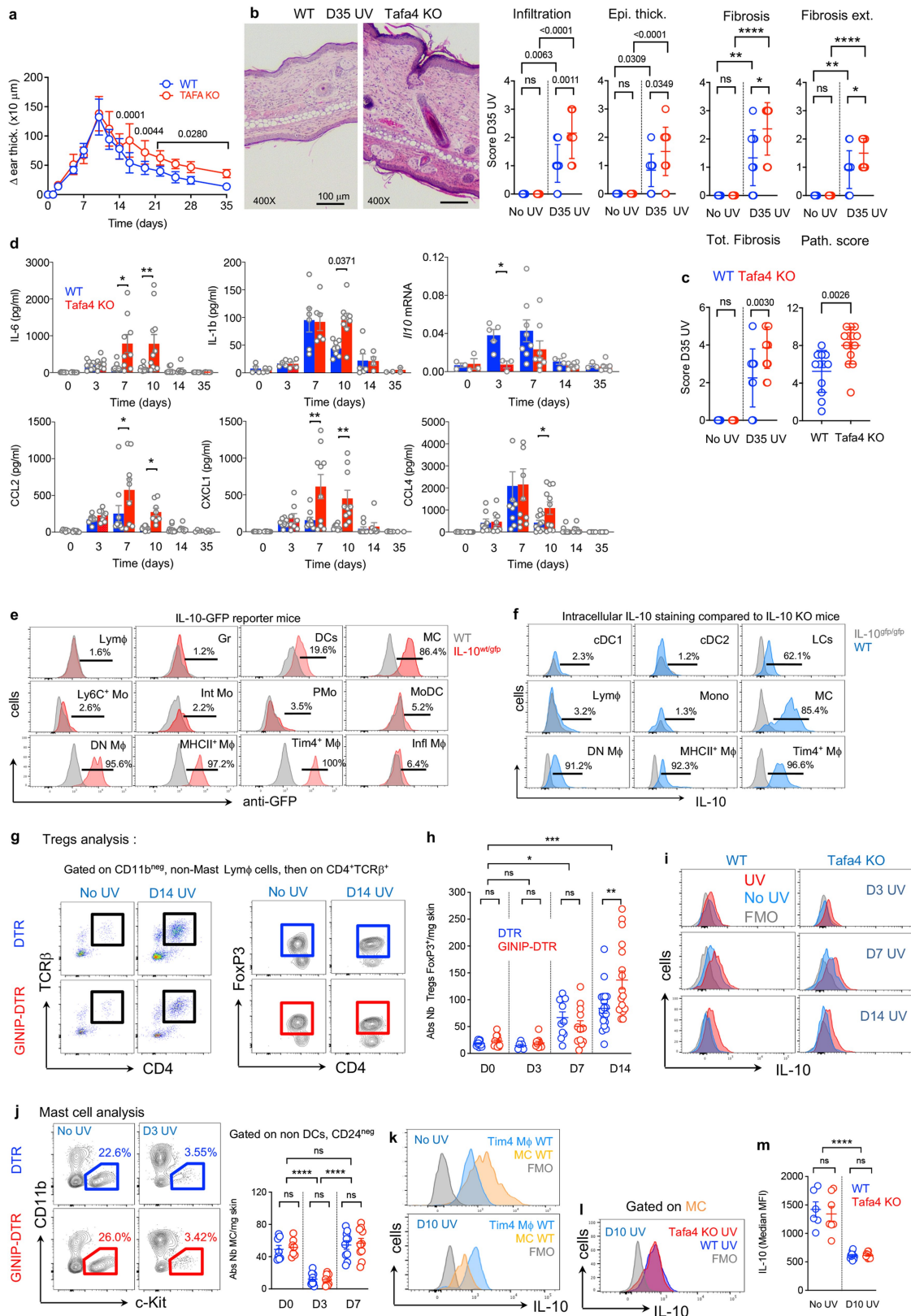
Extended Data Fig. 6 | See next page for caption.

Extended Data Fig. 6 | TAFA4 regulates skin inflammation after UV exposure but does not affect IL-10 production in T_{reg} cells and mast cells. **a**, Changes in ear skin thickness over time post-irradiation in wild-type control (blue) and *Tafa4*-knockout (red) mice (*n* = 9 mice per group). **b**, **c**, Representative H&E images of ears from wild-type (left) or *Tafa4*-knockout (right) mice at D35 post-irradiation and histopathological scoring for leukocyte infiltration, epidermal thickness, fibrosis, fibrosis extension (**b**) and cumulative fibrosis score and total pathological scores (**c**) (*n* = 12 mice per group). See detailed scoring in Methods. **d**, IL-6, IL-1β and chemokines CCL2, CXCL1 and CCL4 levels (measured by CBA) and *Il10* mRNA level, in ear skin from wild-type (blue) or *Tafa4*-knockout (red) mice from D0 to D35 post-irradiation (*n* = 3–11 mice per group and time point). **e**, **f**, FACS analysis and detection of IL-10+ immune cells from control (wild-type; grey) and *IL-10*GFP/WT (red) mice using an anti-GFP antibody (**e**) and using an anti-IL-10 antibody (**f**), in skin dendritic cell subsets, Lymφ cells, monocytes, mast cells (MC) and macrophage subsets in *IL-10*GFP/GFP mice (grey) and wild-type mice (blue). **g**, **h**, Gating strategy for T_{reg} cells (CD4+TCRβ+FoxP3+) (**g**) and absolute number per mg of ear skin before (D0) or post-irradiation, in DTR-control (blue) or GINIP-DTR (red) mice (**h**) (*n* = 9–18 mice per group and per time point). **i**, Representative FACS plots for IL-10 expression in T_{reg} cells from wild-type (left) or *Tafa4*-knockout (right) mice before (blue) or post-irradiation (red). **j**, Gating strategy (left) and absolute number (right) of mast cells (MC) per mg of skin from DTR-control (blue) or GINIP-DTR (red) mice, showing MC depletion (D3) and repopulation (D7) after UV exposure (*n* = 8–9 mice per group and time point). **k**, Representative FACS plots for IL-10 expression in TIM4+ macrophages (blue) and MC (yellow) before (no UV, top) and at D10 post-irradiation (bottom) in wild-type mice. **l**, **m**, Representative FACS plot for IL-10 expression in MC from wild-type (blue) or *Tafa4*-knockout (red) mice at D10 post-irradiation (**l**) and IL-10 median fluorescence intensity (MFI) analysis (*n* = 6–10 mice per group) (**m**). All data are representative of at least two independent experiments and presented as mean ± s.e.m. *P* values determined by one-way ANOVA with Tukey's multiple comparisons test except **a**, two-way ANOVA. NS, not significant; *P < 0.05; **P < 0.01; ***P < 0.001.
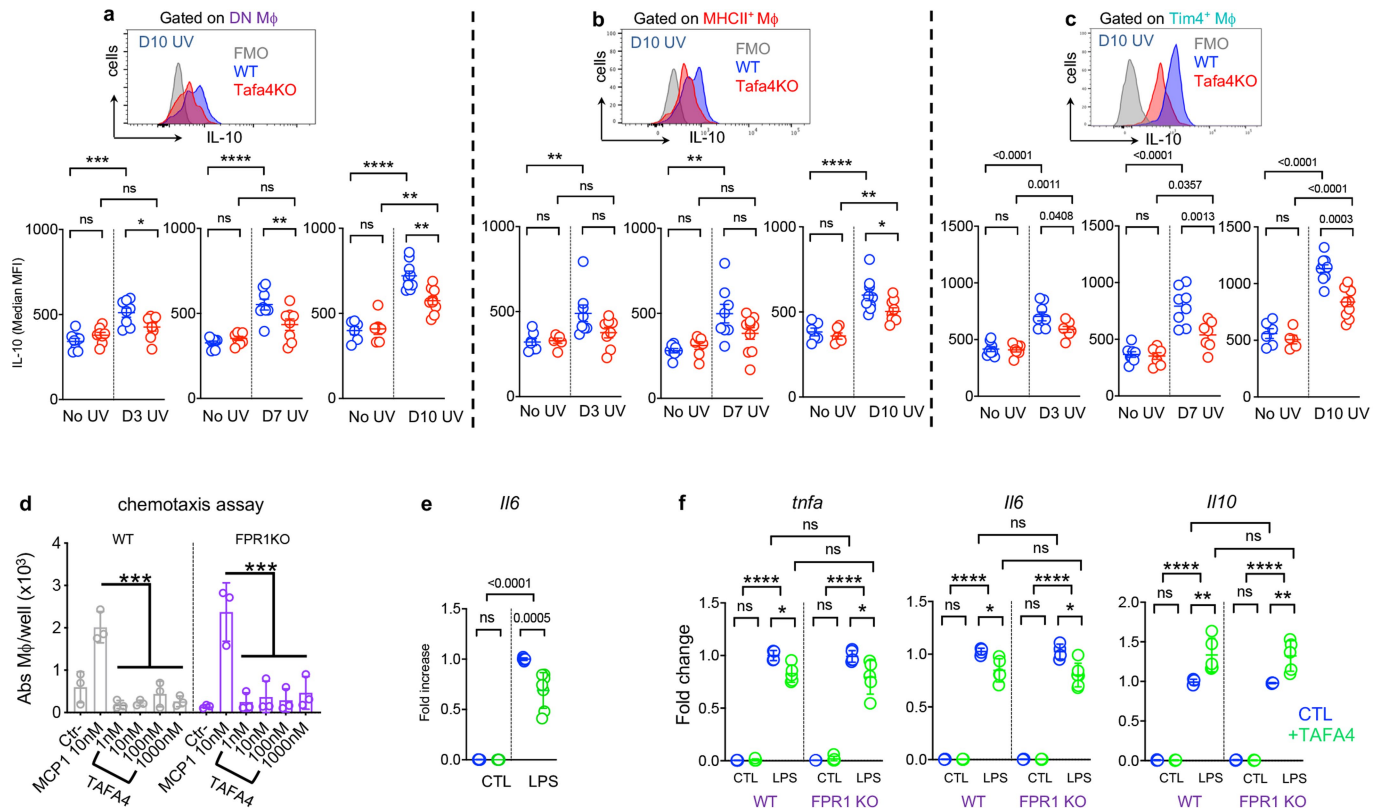
Extended Data Fig. 7 | TAFA4 promotes IL-10 production by dermal resident macrophage subsets in vivo and directly upregulates *Il10* in macrophages in vitro. a–c, Representative FACS plots (top) for intracellular IL-10 expression in DN macrophage (**a**), MHC-II+ macrophage (**b**) and TIM4+ macrophage (**c**) subsets from wild-type (blue) and *Tafa4*-knockout (red) mice at D10 post-irradiation, and IL-10 MFI quantifications (bottom) in the respective macrophage subsets at D3, D7 and D10 post-irradiation (*n* = 6–9 mice per group and time point). **d**, BMDMs, derived from bone marrow of wild-type or *Fpr1*-knockout mice, were challenged in a migration assay (transwell) using medium alone (CTL⁻), MCP-1 (CTL⁺) or increasing concentrations of TAFA4. Absolute number of macrophages in the bottom wells were analysed by FACS (*n* = 3 independent samples per group). **e**, *IL6* mRNA level in thioglycollate-elicited macrophages in the presence (green) or absence (blue) of TAFA4 (related to Fig. 3i) (*n* = 6–8 independent sample per group). **f**, BMDMs as in **d** were activated in vitro by LPS alone (blue) or in the presence of TAFA4 (green). Gene expression was analysed by RT–qPCR for *Tnf*, *Il6* and *Il10* and compared to non-activated BMDM (CTL) (*n* = 4–5 independent samples). All data are representative of at least two independent experiments and presented as mean ± s.e.m. *P* values determined by one-way ANOVA with Tukey's multiple comparisons test. *$P < 0.05$; **$P < 0.01$; ***$P < 0.001$.
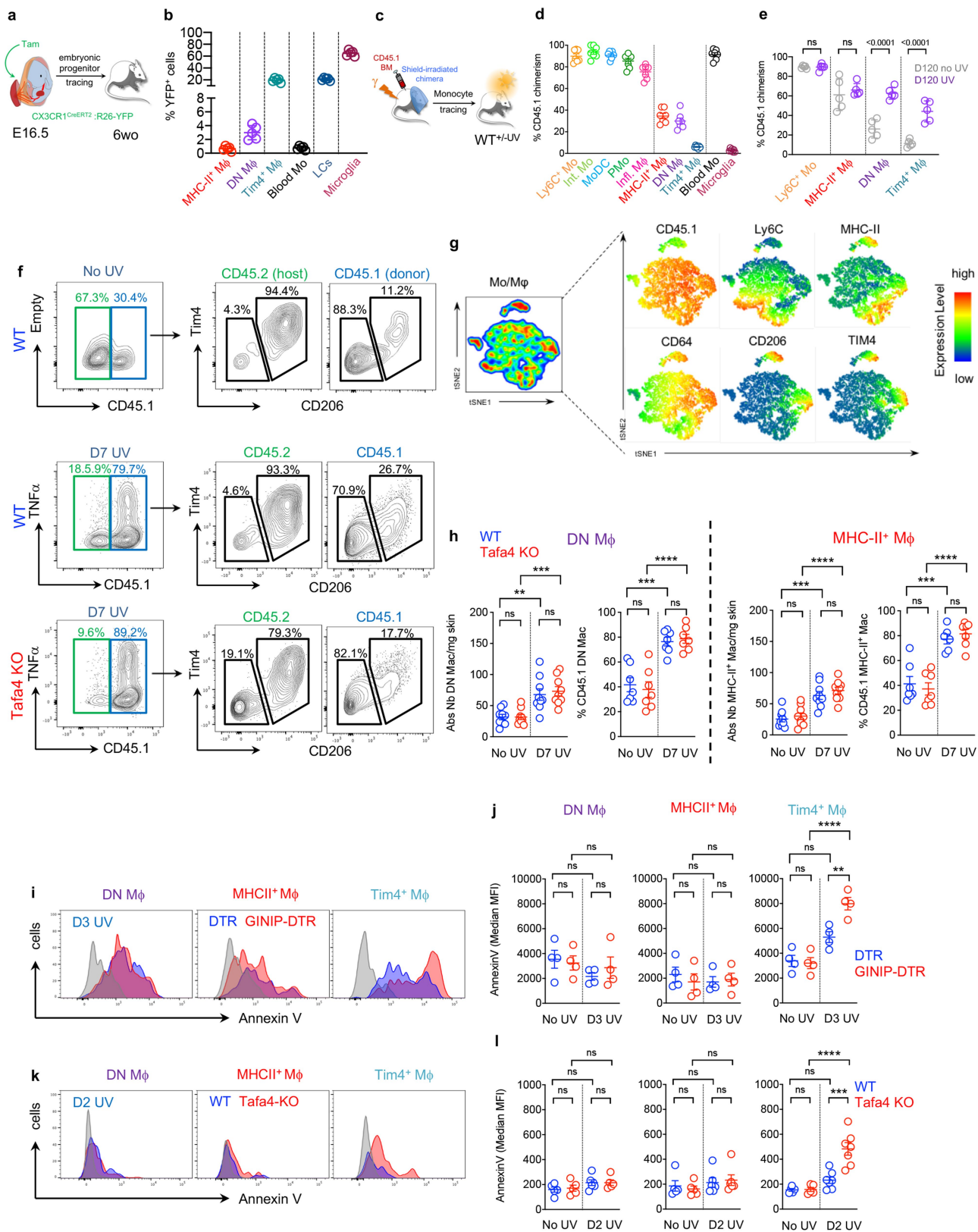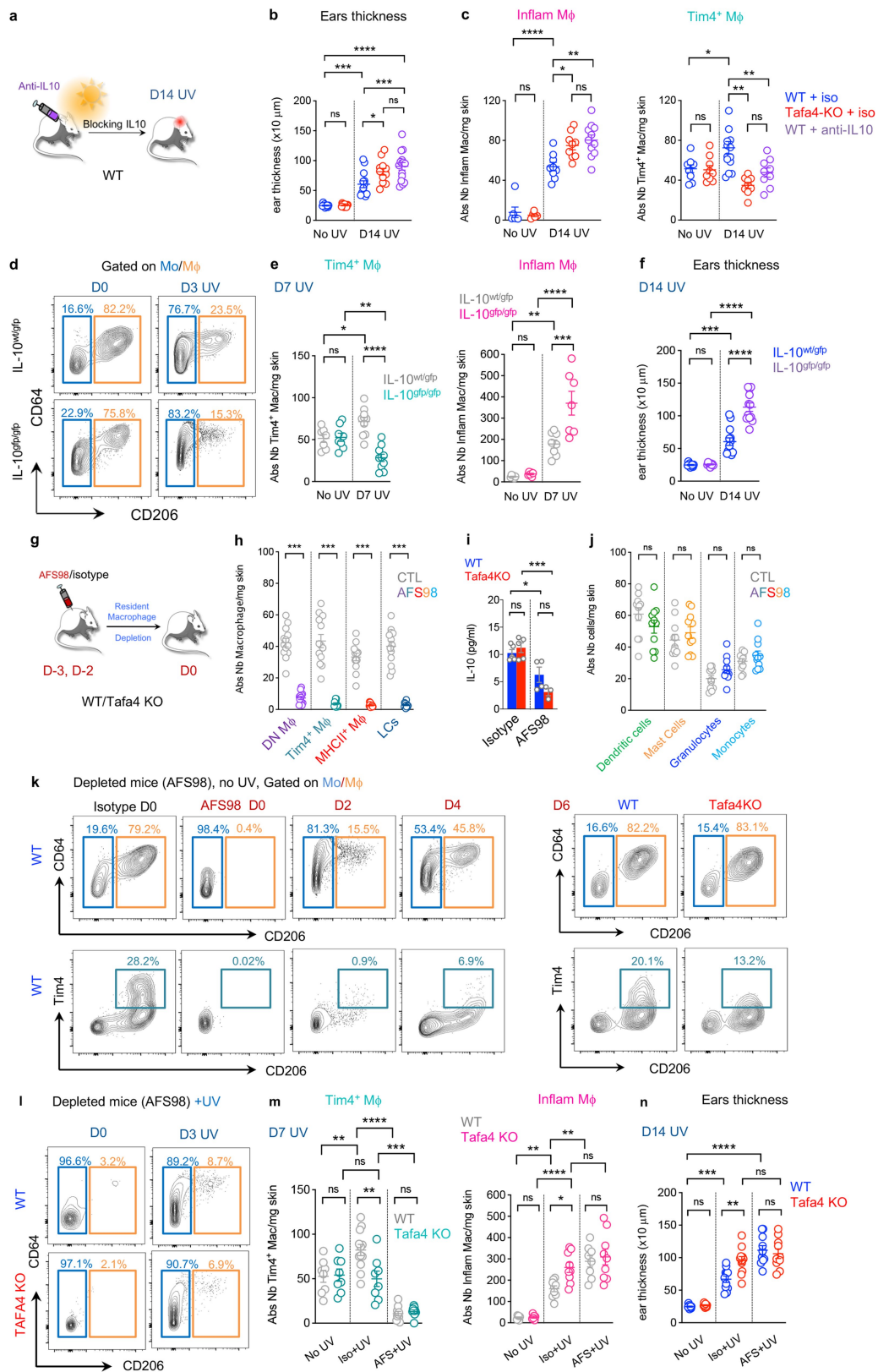
Extended Data Fig. 8 | See next page for caption.

Article

Extended Data Fig. 8 | Fate-mapping and shield-irradiated bone-marrow chimeras revealed that TAFA4 regulates the dynamic between embryo-derived and monocyte-derived macrophages after UV exposure. **a**, Strategy for embryonic progenitor fate mapping using the *CX3CR1*[CreERT2]: *R26-YFP* mice. Tamoxifen (Tam) was injected in pregnant females at E16.5 and offspring were analysed at 6 weeks of age. **b**, Percentages of YFP⁺ cells in the indicated cell types ($n = 5$ mice). LCs, Langerhans cells. **c**, Experimental scheme for monocyte tracing using CD45.1⁺ bone-marrow shield-irradiated chimeras. **d**, **e**, Percentage of CD45.1 chimerism within the indicated monocyte/macrophage subsets in 2-month-old chimeric mice in the steady state ($n = 7$ mice per group) (**d**) or after an additional 4 months following UV irradiation (purple) or no UV irradiation (grey) ($n = 5$ mice per group) (**e**). **f**, Gating strategy for monocyte/macrophage analysis in wild-type CD45.1 bone-marrow chimera before UV exposure (top) and then at D7 post-irradiation in wild-type (middle) and in *Tafa4*-knockout (bottom) recipient chimeras. **g**, Relative expression of the markers CD45.1, Ly6C, CD64, CD206, MHC-II and TIM4 used for *t*-SNE analysis of skin monocyte/macrophage subsets from wild-type or *Tafa4*-knockout recipient chimeras (related to Fig. 4b). **h**, Absolute numbers ($n = 9$ mice per group) per mg of ear skin (left) and CD45.1 chimerism levels (right) ($n = 7$ mice per group) for DN macrophages and MHC-II⁺ macrophages in wild-type (blue) and *Tafa4*-knockout (red) bone-marrow-chimeric mice on D7 post-irradiation. **i**, Representative annexin-V staining of DN macrophages (left), MHC-II⁺ macrophages (middle) and TIM4⁺ macrophages (right) at D3 post-irradiation from DTR (blue) or GINIP-DTR (red) mice. **j**, MFI for annexin-V in macrophage subsets as in **i** ($n = 4$ mice per group). **k**, Representative annexin-V as in **i** at D2 post-irradiation for wild-type (blue) or *Tafa4*-knockout (red) mice. **l**, MFI for annexin-V in macrophage subsets as in **j** ($n = 5$–6 mice per group). All data are representative of at least two independent experiments and presented as mean ± s.e.m. *P* values determined by one-way ANOVA with Tukey's multiple comparisons test. NS, not significant; *$P < 0.05$; **$P < 0.01$; ***$P < 0.001$.
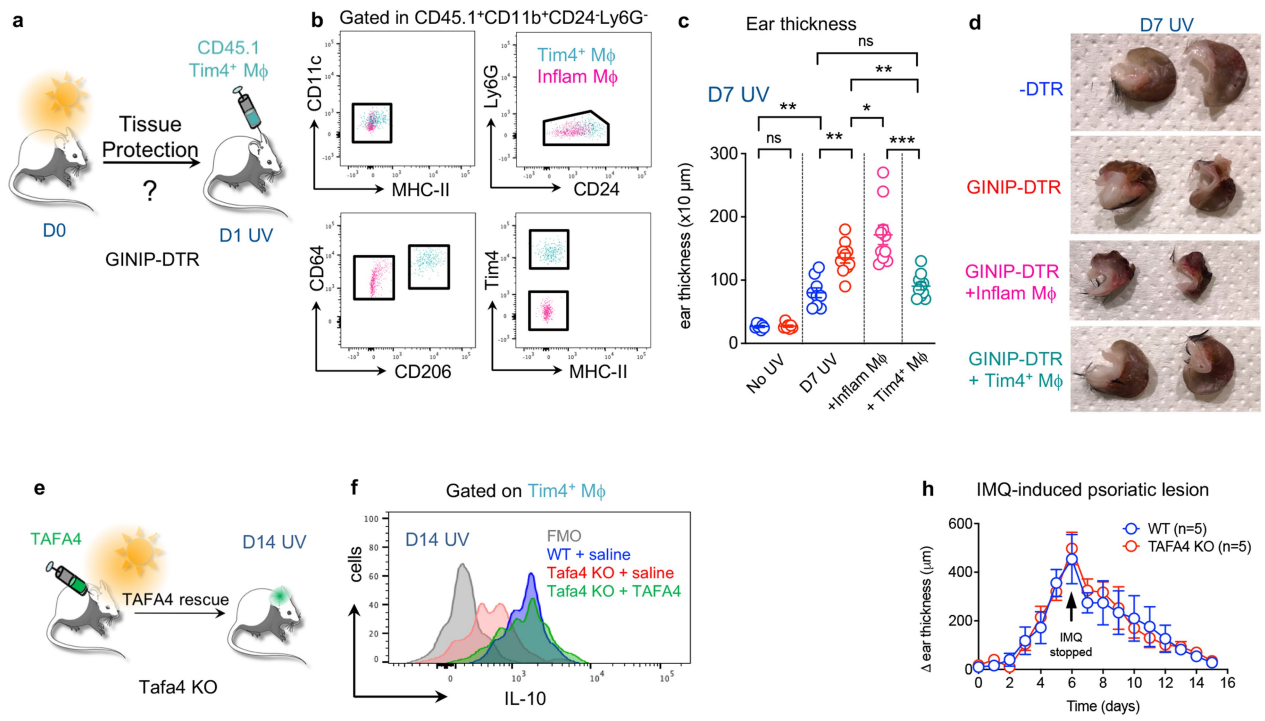
Extended Data Fig. 9 | See next page for caption.

Article

Extended Data Fig. 9 | IL-10 defect and dermal macrophage depletion recapitulate the *Tafa4*-knockout mouse phenotype after UV exposure.
a, Experimental scheme for in vivo neutralization of IL-10 in wild-type mice.
b, Ear thickness, at D14 post-irradiation, of wild-type (blue) or *Tafa4*-knockout (red) mice treated with an IgG2a isotype control (iso) and of wild-type mice treated with anti-IL-10 blocking antibodies (purple) ($n = 10$ mice per group).
c, Absolute numbers of inflammatory macrophages (left) and TIM4$^+$ macrophages (right) in the ear skin of the indicated 3 groups of mice (as in **b**) ($n = 6$–9 mice per group). **d**, Representative FACS plots of monocyte/macrophage subsets at D0 and D3 post-irradiation in *IL-10*$^{WT/GFP}$ and *IL-10*$^{GFP/GFP}$ (*Il10*-knockout) mice. **e**, Absolute number of TIM4$^+$ macrophages (left) and inflammatory macrophages (right) per mg of skin at D7 post-irradiation in *IL-10*$^{WT/GFP}$ (grey) and *IL-10*$^{GFP/GFP}$ (coloured) ($n = 8$–10 mice per group). **f**, Ear thickness before (no UV) and at D14 post-irradiation (UV) in *IL-10*$^{WT/GFP}$ (blue) and *IL-10*$^{GFP/GFP}$ (purple) mice ($n = 9$–12 mice per group). **g**, Experimental scheme for dermal resident macrophage depletion: two i.p. injections, at 3 days (D − 3) and 2 days (D − 2) before D0, of the CSF-1R blocking antibody AFS98, are effective to deplete DN, TIM4$^+$, MHC-II$^+$ and Langerhans cells in wild-type mice.
h, Absolute number of macrophages per mg of ear skin before (CTL) and after AFS98 injection (coloured) ($n = 13$ mice per group). **i**, IL-10 level detected by CBA in wild-type (blue) a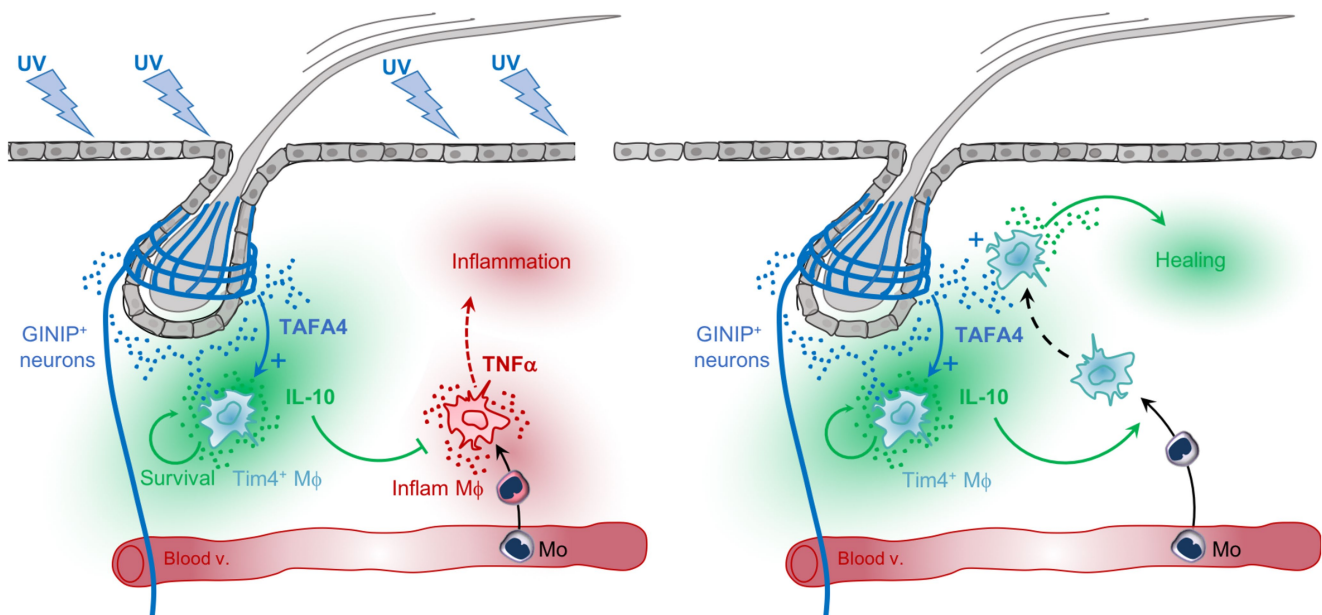nd *Tafa4*-knockout (red) mice after isotype control or AFS98 antibody injection ($n = 4$–5 mice per group). **j**, Absolute number of myeloid cell subsets per mg of ear skin after isotype control or AFS98 antibody injection (coloured) ($n = 11$ mice per group). **k**, Left, representative FACS plots of monocyte/macrophage subsets over the time course of macrophage repopulation (D0, D2 and D4) after AFS98 injection and complete macrophage depletion (D0) in wild-type mice; right, representative FACS plots at D6 after AFS98 injection in wild-type (blue) and *Tafa4*-knockout (red) mice showing the acquisition of TIM4 by monocyte-derived macrophages (see bottom panels).
l, Representative FACS plots of monocyte/macrophage subsets at D0 and D3 post-UV exposure in wild-type and *Tafa4*-knockout mice after macrophage depletion with the blocking anti-CSF-1R antibody (AFS98). **m**, Absolute number of TIM4$^+$ macrophages (left) and inflammatory macrophages (right) per mg of skin at D7 post-irradiation in wild-type (grey) and *Tafa4*-knockout (coloured) mice treated with an IgG2a isotype control (Iso+UV), or treated with anti-CSF-1R antibody (AFS+UV) ($n = 8$–9 mice per group). **n**, Ear thickness in unexposed mice (no UV), and at D14 post-irradiation in wild-type (blue) and *Tafa4*-knockout (red) mice treated as in **m** ($n = 10$ mice per group). All data are representative of at least two independent experiments and presented as mean ± s.e.m. *P* values determined by one-way ANOVA with Tukey's multiple comparisons test. NS, not significant; *$P < 0.05$; **$P < 0.01$; ***$P < 0.001$.

a Tissue Protection ? — D0 GINIP-DTR → D1 UV, CD45.1 Tim4⁺ Mφ

b Gated in CD45.1⁺CD11b⁺CD24⁻Ly6G⁻

- CD11c vs MHC-II
- Ly6G vs CD24 — Tim4⁺ Mφ / Inflam Mφ
- CD64 vs CD206
- Tim4 vs MHC-II

c Ear thickness

D7 UV — ear thickness (x10 µm)
Groups: No UV, D7 UV, +Inflam Mφ, + Tim4⁺ Mφ

d D7 UV
- -DTR
- GINIP-DTR
- GINIP-DTR +Inflam Mφ
- GINIP-DTR + Tim4⁺ Mφ

e TAFA4 → UV → D14 UV, TAFA4 rescue, Tafa4 KO

f Gated on Tim4⁺ Mφ

D14 UV — cells vs IL-10
- FMO
- WT + saline
- Tafa4 KO + saline
- Tafa4 KO + TAFA4

h IMQ-induced psoriatic lesion

Δ ear thickness (µm) vs Time (days)
- WT (n=5)
- TAFA4 KO (n=5)
- IMQ stopped

g Model

1) Role of TAFA4 during the Inflammatory phase

GINIP⁺ neurons, TAFA4 +, IL-10, Survival, Tim4⁺ Mφ, Inflammation, TNFα, Inflam Mφ, Mo, Blood v.

2) Role of TAFA4 during the Resolution phase

GINIP⁺ neurons, TAFA4 +, IL-10, Healing, Tim4⁺ Mφ, Mo, Blood v.

Extended Data Fig. 10 | See next page for caption.

Extended Data Fig. 10 | Adoptive transfer of TIM4⁺ macrophages is sufficient to reduce tissue damage in GINIP-DTR mice. a, Experimental scheme for intradermal adoptive transfer of CD45.1⁺TIM4⁺ macrophages. **b**, Gating strategy for sorting CD45.1⁺ inflammatory macrophages (pink) and TIM4⁺ macrophages (cyan). **c**, Ear thickness for unexposed (no UV) or UV-exposed mice at D7 post-irradiation, in DTR (blue), GINIP−DTR (red) mice and GINIP-DTR mice injected with inflammatory macrophages (pink) or with TIM4⁺ macrophages (cyan) (n = 7–10 mice per group). **d**, Representative images of ears at D7 post-irradiation from each group as in **c**. **e**, Experimental scheme for TAFA4 rescue in *Tafa4*-knockout mice. **f**, Representative FACS plot for intracellular staining of IL-10 in TIM4⁺ macrophages at D14 post-irradiation, in wild-type mice treated with saline (blue) or *Tafa4*-knockout mice treated with saline (red) or *Tafa4*-knockout mice treated with TAFA4 (green). **g**, Model for TAFA4 functions in vivo after UV exposure: (1) role of TAFA4 during the inflammatory phase. Skin overexposure to UV induces the release of the neuropeptide TAFA4 by C-LTMRs. TAFA4 promotes the production of IL-10 by embryonic-derived dermal resident TIM4⁺ macrophages. The production of IL-10 is essential for their survival and protect the skin from over-inflammation. Tissue lesions also induce the recruitment of monocytes in the skin, where they differentiate into TNF⁺ inflammatory macrophages. In the absence of TAFA4 production, the number of TIM4⁺ macrophages and IL-10 levels are reduced, promoting the expansion of inflammatory macrophages. (2) Role of TAFA4 during the resolution phase. The TAFA4−IL-10 axis is still active, promoting the maintenance of both embryonic- and monocyte-derived IL-10⁺ TIM4⁺ macrophages, which are required for tissue repair. In the absence of TAFA4 production, IL-10 production by the three subsets of CD206⁺ dermal macrophages, is compromised, leading to persistent inflammation and fibrotic scars. **h**, Repeated measure over time of ear thickness changes (μm) of wild-type (blue) and *Tafa4*-knockout (red) mice treated daily with imiquimod (IMQ) during six consecutive days and followed up to 15 days (n = 5 mice per group). All data are representative of at least two independent experiments and presented as mean ± s.e.m. P values determined by one-way ANOVA with Tukey's multiple comparisons test. NS, not significant; *P < 0.05; **P < 0.01; ***P < 0.001.

Corresponding author(s): Sophie Ugolini; Guillaume Hoeffel

Last updated by author(s): 11/04/2021

Reporting Summary

Nature Research wishes to improve the reproducibility of the work that we publish. This form provides structure for consistency and transparency in reporting. For further information on Nature Research policies, see Authors & Referees and the Editorial Policy Checklist.

Statistics

For all statistical analyses, confirm that the following items are present in the figure legend, table legend, main text, or Methods section.

n/a	Confirmed	
☐	☒	The exact sample size (n) for each experimental group/condition, given as a discrete number and unit of measurement
☐	☒	A statement on whether measurements were taken from distinct samples or whether the same sample was measured repeatedly
☐	☒	The statistical test(s) used AND whether they are one- or two-sided *Only common tests should be described solely by name; describe more complex techniques in the Methods section.*
☐	☒	A description of all covariates tested
☐	☒	A description of any assumptions or corrections, such as tests of normality and adjustment for multiple comparisons
☐	☒	A full description of the statistical parameters including central tendency (e.g. means) or other basic estimates (e.g. regression coefficient) AND variation (e.g. standard deviation) or associated estimates of uncertainty (e.g. confidence intervals)
☐	☒	For null hypothesis testing, the test statistic (e.g. F, t, r) with confidence intervals, effect sizes, degrees of freedom and P value noted *Give P values as exact values whenever suitable.*
☒	☐	For Bayesian analysis, information on the choice of priors and Markov chain Monte Carlo settings
☒	☐	For hierarchical and complex designs, identification of the appropriate level for tests and full reporting of outcomes
☒	☐	Estimates of effect sizes (e.g. Cohen's d, Pearson's r), indicating how they were calculated

Our web collection on statistics for biologists contains articles on many of the points above.

Software and code

Policy information about availability of computer code

Data collection	NA
Data analysis	ZEN lite software (v2.6), Adobe Photoshop CS6, ImageJ (v1.52), GraphPad Prism (v7), FlowJo

For manuscripts utilizing custom algorithms or software that are central to the research but not yet described in published literature, software must be made available to editors/reviewers. We strongly encourage code deposition in a community repository (e.g. GitHub). See the Nature Research guidelines for submitting code & software for further information.

Data

Policy information about availability of data

All manuscripts must include a data availability statement. This statement should provide the following information, where applicable:

- Accession codes, unique identifiers, or web links for publicly available datasets
- A list of figures that have associated raw data
- A description of any restrictions on data availability

Data are available from the corresponding author on reasonable request.

Field-specific reporting

Please select the one below that is the best fit for your research. If you are not sure, read the appropriate sections before making your selection.

☒ Life sciences   ☐ Behavioural & social sciences   ☐ Ecological, evolutionary & environmental sciences

For a reference copy of the document with all sections, see nature.com/documents/nr-reporting-summary-flat.pdf

Life sciences study design

All studies must disclose on these points even when the disclosure is negative.

Sample size	No statistical methods were used to predetermine sample size. For genetic and knockout models at least n=3 mice per group from 2 independent litters were analyzed.
Data exclusions	Outliers were identified and excluded using the ROUT method with Q=1% on GraphPad Prism
Replication	All attempts for replication were successfully performed by multiple investigators using independent litters of mice.
Randomization	Male and female littermates were assigned into the control or knockout groups after genotyping
Blinding	The investigators were not blinded to allocation during following experiments and outcome assessment.

Reporting for specific materials, systems and methods

We require information from authors about some types of materials, experimental systems and methods used in many studies. Here, indicate whether each material, system or method listed is relevant to your study. If you are not sure if a list item applies to your research, read the appropriate section before selecting a response.

Materials & experimental systems

n/a	Involved in the study
☐	☒ Antibodies
☒	☐ Eukaryotic cell lines
☒	☐ Palaeontology
☐	☒ Animals and other organisms
☒	☐ Human research participants
☒	☐ Clinical data

Methods

n/a	Involved in the study
☒	☐ ChIP-seq
☐	☒ Flow cytometry
☒	☐ MRI-based neuroimaging

Antibodies

Antibodies used	All antibodies were published, and titrated prior to initial experiments. Clones, associated fluorophores and dilutions are listed in the Article Methods Anti-mouse F4/80-PECF594 (BD; #565613) Anti-mouse CD45.1-BV605 (BD; #747743) Anti-mouse CD11b-BV510 (BD; #562950) Anti-mouse CD11c-BUV395 (BD; #744180) Anti-mouse CD24-BUV737 (BD; #612832) Anti-mouse CD4 PE-Cy7 (BD; #552775) Anti-mouse TCRbeta APC-Cy7 (BD; #560656) Anti-mouse Ly6C-BV421 (BD; #562727) Anti-mouse Ly6G-APC-Cy7 (BD; #560600) Anti-mouse CD45-BV785 (Biolegend; #BLE109839) Anti-mouse CD64-BV711 (Biolegend; #BLE139311) Anti-mouse EpCAM-AF594 (Biolegend; #BLE118222) Anti-mouse CD206-APC (Biolegend; #BLE141708) Anti-mouse Tim4-PeCy7 (Biolegend; #BLE130010) Anti-mouse CD117-BV605 (Biolegend; #BLE105847) Anti-mouse CD103-PerCP-Cy5.5 (Biolegend; #BLE121416) Mouse TNFa CBA Flex Set, bead C8 (BD; #558299) Mouse IL-1beta CBA Flex Set, bead E5 (BD; #560232) Mouse IL-10 CBA Enhanced Sensitivity Flex Set, bead C4 (BD; #562263) Mouse IL-6 CBA Flex Set, bead B4 (BD; #558301) Mouse CCL2 CBA Flex Set, bead B7 (BD; #558342) Mouse CXCL1 CBA Flex Set, bead A9 (BD; #558340) Mouse CCL4 CBA Flex Set, bead C9 (BD; #558343) Anti-mouse TNFa-PE (BD; #554419) Anti-mouse IL-10-PE (BD; #559063) Anti-mouse CCR2-PE (R&D; #FAB5538P-100) Mouse IL-10 neutralizing antibody (R&D; #MAB1835-500) Anti-human DTR (anti-hHB-EGF; R&D; #AF-259-NA), Anti-GFP, polyclonal Rabbit-A488 (Invitrogen; #A-21311) Anti-mouse IA/I-E-AF700 (eBioscience; #56-5321-82) Anti-mouse IL-1beta-PE (eBioscience; #12-7114-82) anti-mouse FoxP3-A488 1:200 (eBioscience; #53-4777-42)

Anti-mouse CD207-APC (Dendritics; #DDX0362)
Donkey anti-mouse-A594 (Jackson Immunoresearch; #715-585-151)
Donkey anti-rat-A488 (Jackson Immunoresearch; #712-545-153)
Donkey anti-rabbit-A594 (Jackson Immunoresearch; #711-585-152)
Donkey anti-goat-A647 (Jackson Immunoresearch; #705-605-147)
Anti-TH antibody (Merck Millipore; #AB152)
Anti-ATF3 antibody (Abcam; #207434)
Anti-mouse CD16/32 (Fc block), (BD; #553142)
Anti-mouse CGRP (Abcam; #ab36001)

Validation	The anti-GINIP was generated in the A. Moqrich lab as described in the method section. The anti-TAFA4 monoclonal antibodies were generated by MImAbs (https://www.mimabs.org) as described in the paper. All the other antibodies used are commercially available as decribed in the manuscript. We selected antibody clones that have been extensively used in the literature. We also titrated all antibodies prior to experiments.

Animals and other organisms

Policy information about studies involving animals; ARRIVE guidelines recommended for reporting animal research

Laboratory animals	All ages are listed in the text when the animal was used, and additional information is located in the Article Methods section under mice.
Wild animals	NA
Field-collected samples	NA
Ethics oversight	All experiments were conducted in accordance with institutional committee recommendations (Comité d'Ethique de Marseille no. 14-APAFiS # 18469-2019011417196625v2) and French and European guidelines for animal care.

Note that full information on the approval of the study protocol must also be provided in the manuscript.

Flow Cytometry

Plots

Confirm that:

☒ The axis labels state the marker and fluorochrome used (e.g. CD4-FITC).

☒ The axis scales are clearly visible. Include numbers along axes only for bottom left plot of group (a 'group' is an analysis of identical markers).

☒ All plots are contour plots with outliers or pseudocolor plots.

☒ A numerical value for number of cells or percentage (with statistics) is provided.

Methodology

Sample preparation	For flow cytometry experiments, skin samples were collected and finely minced with scissor in complete medium (RPMI+L-Glutamine, 10% FCS) and incubated 1h at 37°C with 1mg/ml DNase (Roche) 0.2ml/ml Dispase (GIBCO) and 0.2mg/ml collagenase type IV (Sigma). Tissues were then dissociated using 2.5 ml syringes and 18G needles and filtered on cell strainer. Cells were then washed in FACS buffer (PBS-2mM EDTA, FCS 2%). Cell suspensions were centrifuged at 1300rpm for 4 min, resuspended in FACS buffer (PBS, 0.5% BSA and 2 mm EDTA) containing purified anti-CD16/32 (1:100 dilution) and immunostained with antibodies mixes for 45 min at 4ºC.
Instrument	LSRFortessa X20 (BD)
Software	Data was collected using DiVa 8.0.1 Software. Subsequent analysis was performed with FlowJo_v9.9.4. and v10.4
Cell population abundance	NA
Gating strategy	FSC/SSC gates and dead cell stain (live/dead fixable blue Dead Cell Stain kit UV; L23105; Invitrogen). were used to define single live cells. Doublets were removed based on FSCA/FSC-W. In primary experiments all gates were defined based on FMO controls. In consecutive experiments, gates in fluorescence channels were drawn based on clear separation between negative and positive populations.

☒ Tick this box to confirm that a figure exemplifying the gating strategy is provided in the Supplementary Information.